Mapping *Plasmodium* transitions and interactions in the *Anopheles* female

Yan Yan[1]*, Elaine Cheung[1]*, Lisa H. Verzier[1]*, Federico Appetecchia[1], Sandra March[2,3,4,5], Ailsa R. Craven[1], Esrah Du[1], Alexandra S. Probst[1], Tasneem A. Rinvee[1], Laura E. de Vries[1], Jamie Kauffman[1], Sangeeta N. Bhatia[2,3,4,5,6], Elisabeth Nelson[1], Naresh Singh[1], Duo Peng[1,7], W. Robert Shaw[1,2], Flaminia Catteruccia[1,2,#]

[1] Department of Immunology and Infectious Disease, Harvard T. H. Chan School of Public Health, Boston, MA 02115, USA.

[2] Howard Hughes Medical Institute, Boston, MA 02115, USA.

[3] Institute for Medical Engineering and Science, Massachusetts Institute of Technology (MIT), Cambridge, MA 02139, USA.

[4] David H. Koch Institute for Integrative Cancer Research, MIT, Cambridge, MA 02139, USA.

[5] Broad Institute of MIT and Harvard, Cambridge, MA 02139, USA.

[6] Wyss Institute at Harvard University, 201 Brookline Ave, Boston, MA 02215, USA

[7] Current address: The Chan Zuckerberg Biohub, San Francisco, CA 94158, USA.

* These authors contributed equally

[#] Corresponding author: fcatter@hsph.harvard.edu

Abstract

The human malaria parasite, *Plasmodium falciparum*, relies on *Anopheles* mosquitoes for transmission. Once ingested during blood feeding, most parasites die in the mosquito midgut lumen or during epithelium traversal. How surviving ookinetes interact with midgut cells and form oocysts is unknown, yet these steps are essential to initiate a remarkable, similarly uncharacterized growth process culminating in the production of thousands of infectious sporozoites. Here, using single-cell RNA sequencing of both parasites and mosquito cells across four time points and two metabolic conditions, we unveil key processes shaping developmental transitions and mosquito-parasite interactions occurring in the midgut. In depth functional analyses reveal processes regulating oocyst growth and identify the transcription factor *Pf*SIP2 as essential for sporozoite infection of human hepatocytes. By combining the analysis of shared mosquito-parasite barcodes with confocal microscopy, we discover that parasites preferentially interact with midgut progenitor cells during epithelial crossing, potentially using their basal location as an exit landmark. Additionally, we unveil tight connections between extracellular late oocysts and surrounding muscle cells that may ensure parasites adhere to the midgut without damaging it. Ultimately, our study provides fundamental insight into the molecular events characterizing previously inaccessible biological transitions and mosquito-parasite interactions, and identifies candidates for transmission-blocking strategies.

Introduction

The apicomplexan parasite *Plasmodium falciparum* is responsible for 90% of malaria cases, a disease that in 2022 alone caused the death of over 600,000 people, mostly in sub-Saharan Africa [1]. Like all malaria parasites, *P. falciparum* requires a blood-feeding vector for transmission between humans, and over the course of a long co-evolutionary history has adapted to be exclusively transmitted by mosquitoes of the *Anopheles* genus. The journey of the parasite in the *Anopheles* female [2] starts when male and female gametocytes are ingested during a bloodmeal and rapidly mature into gametes, leading to fertilization and formation of a zygote which transforms into a motile ookinete in the blood bolus. Between 24-36 hours after ingestion, ookinetes cross the midgut epithelium to avoid killing during blood digestion. These initial steps lead to large losses of parasites, making ookinete formation and midgut crossing one of the most severe bottlenecks in the parasite lifecycle [3]. Once the ookinete reaches the basal side of the midgut, it rounds up via an intermediate took stage ('**t**ransition from **ook**inete') [4] to transform into an extracellular oocyst, which over the next 7–10 days will extensively grow in size just underneath the basal lamina surrounding the midgut epithelial layer while undergoing rapid DNA replication. This remarkable growth process culminates in the formation of thousands of infectious sporozoites, an intricate process where individual parasites must be segmented precisely over a relatively short period of time [5] (Figure 1a). When mature, sporozoites egress from the oocyst and invade the mosquito salivary glands, whereby they can be transmitted to the next person when the mosquito bites again.

The mosquito stages of *P. falciparum* development are considerably unexplored despite their essential role in sustaining transmission, and current knowledge is largely extrapolated from work on more tractable rodent malaria models [6-8]. While several studies have analyzed ookinete invasion of the midgut epithelium [9-13], whether parasites interact with specific midgut cell types and the mechanisms that trigger their transition into oocysts remain largely unknown. The processes fueling oocyst development and ensuring sporozoite formation are also barely uncovered. Tackling these questions has been challenging due to the necessity to study mosquito stages of *P. falciparum in vivo*, combined with a paucity of effective genetic tools compared to asexual blood stage parasites [14]. Compounding these issues is the bottleneck in mosquitoes, as midguts contain a notably limited number of parasites. As a consequence, single-cell RNA sequencing (scRNA-seq) studies have focused on mosquito stages where parasites are numerous and readily isolated (i.e. gametes and blood bolus

ookinetes, and fully formed sporozoites isolated from oocysts, hemolymph and salivary glands) [15, 16], leaving significant gaps in the parasite life cycle.

Here, we reconstruct critical bottleneck stages of parasite growth and unveil novel mosquito-parasite interactions in the midgut by performing dual single-cell RNA sequencing (scRNA-seq) of parasites and midgut cells over time, capturing key processes mediating midgut crossing, oocyst growth, and sporozoite formation.

Results

ScRNA-seq of midgut and parasite cells

We infected *Anopheles gambiae* – the major malaria vector in sub-Saharan Africa – with *P. falciparum* and isolated both parasites and midgut cells at 4 different time points: invading ookinetes that are transforming into oocysts (36 hours post infection, h pi); newly formed oocysts (2 days pi, d pi); oocysts that are growing (4d pi) and oocysts that are well advanced in the growth phase and may have begun sporozoites segmentation (7d pi) (Figure 1a; Supplementary Figure 1a). Due to the exceedingly low numbers of parasites in these stages relative to the overwhelming number of mosquito cells [17], we enriched for parasites by meticulously optimizing the single-cell isolation protocol (see methods) and applied deeper sequencing. We compared parasites developing in mosquitoes under two metabolic conditions: control mosquitoes (injected with double-stranded RNA against *eGFP*, ds*GFP*) and mosquitoes depleted of the Ecdysone Receptor (ds*EcR*), the nuclear co-receptor of the steroid hormone 20-hydroxy-ecdysone (20E) [18, 19] (Supplementary Figure 1b-e). As impairing 20E signaling affects midgut metabolism after blood feeding, reliably accelerating oocyst growth and leading to earlier sporozoite formation, we reasoned that comparing these conditions would provide increased resolution at later stages of parasite development [18, 20]. After quality control, we successfully profiled 3,495 parasites, detecting a median of 242-1,773 genes at the various time points and treatments (Supplementary Figure 1f, Supplementary Table 1).

Principal component analysis (PCA) revealed a large separation between the majority of parasites along the first component, with parasites at 2, 4 and 7d pi clustering away from the bulk of the 36h pi parasites (Figure 1b). This substantial shift observed as parasites transition from the invasive to the growth phase was reflected by differential gene expression comparisons between time points, which showed downregulation of RNA metabolism along with upregulation of translation after ookinete invasion (2d vs. 36h), and upregulation of aerobic respiration during oocyst formation and growth (4d vs. 2d) (Supplementary Figure 2,

106 Supplementary Table 2). PCA at early time points showed no clear separation between
107 parasites developing in ds*GFP* and ds*EcR* mosquitoes, and we detected limited differences in
108 gene expression between these groups. Parasite numbers were also similar, as previously
109 observed after *EcR* silencing at low parasite densities [20] (Figure 1b, Supplementary
110 Figure 1b, 2a). At 7d pi, however, parasites from ds*EcR* females showed several upregulated
111 genes (Supplementary Figure 2b, c, Supplementary Table 2) likely reflecting the more
112 advanced growth of oocysts in this group (Supplementary Figure 1c). Among these genes were
113 the circumsporozoite protein (CSP, the most abundant sporozoite surface protein), and genes
114 from the rhoptries, secretory organelles essential for invasion of host cells [21, 22]. These
115 signals suggest we had succeeded in capturing a subset of parasites at the start of sporozoite
116 segmentation.
117
118 **Gene network analysis over pseudotime**
119 Next, we generated a Uniform Manifold Approximation and Projection (UMAP)
120 encompassing a complete atlas of parasites in the mosquito midgut by integrating our data with
121 blood bolus (BB) gametes and ookinetes, and sporozoites isolated from oocysts from two
122 previous scRNA-seq studies [15, 16] (Figure 1c). The resulting UMAP nicely enclosed our data
123 and uncovered 11 clusters, which we annotated based on marker genes and data source as
124 follows: Gametes/Zygotes, BB ookinetes, invading ookinetes (Ookinete 1 and 2), the ookinete-
125 oocyst transition stage (Took), newly formed oocysts (d2 oocyst), growing oocysts (Oocyst 1-
126 4) and oocysts that are segmenting into sporozoites (Oocyst spz) (Figure 1d-e, Supplementary
127 Figure 3a, Supplementary Table 3). In agreement with the previous observation of early
128 segmentation signals at 7d pi, a few cells bridged the gap between oocysts that were in the
129 advanced growth phase and sporozoites isolated from oocysts (Figure 1c, Supplementary
130 Figure 3b).
131 Pseudotime analysis revealed a single trajectory aligning with the expected clusters
132 (Figure 1f). We clustered genes with similar expression patterns over pseudotime, limiting this
133 analysis to our data due to differences in gene detection rates among scRNA-seq techniques.
134 This analysis identified 15 gene clusters separating into four major branches (Figure 1g,
135 Supplementary Table 4). The first main branch (gene clusters 6, 9) captured expected
136 differences between BB ookinetes and ookinetes that are crossing the epithelium. Specifically,
137 cluster 6, which was more highly expressed in BB parasites, was associated with ookinete
138 maturation and characterized by genes involved in cytoskeleton and myosin complex [23].

139 Conversely, cluster 9, expressed across all ookinete clusters, comprised micronemal proteins
140 critical for motility and midgut traversal, such as circumsporozoite-and TRAP-related protein
141 (CTRP), chitinase, and glycosylphosphatidylinositol-anchored micronemal antigen (GAMA)
142 [24, 25].

143 The second branch revealed processes related to surface remodeling and adhesion as
144 well as gene transcription. Interestingly, the expression of these genes corresponds to the
145 ookinete-oocyst transition, a yet uncharacterized process during which parasites undergo
146 profound morphological changes. A strong signal related to gene expression with helicase
147 activity and RNA processing – including splicing – were found at the onset of this transition in
148 cluster 13 and 2. Cluster 2, as well as 5, also encompassed membrane and vesicle trafficking
149 genes which may facilitate protein transport and surface remodeling, while cluster 13 and 11
150 contained several *var* genes encoding variants of *Pf*EMP1 proteins, well characterized for their
151 adhesion properties in the asexual blood stage [26]. It is intriguing to speculate that young
152 oocysts may use *Pf*EMP1 to anchor themselves between midgut cells and basal lamina.

153 The largest branch showed expression from d2 oocysts to Oocyst spz and captured the
154 processes fueling the growth phase. This branch contained genes related to translation,
155 proteasome activity, and ribonucleoprotein complex (clusters 12, 8 and 7) as well as genes
156 related to aerobic respiration, lipid biosynthesis, and apicoplast organelle (clusters 8, 1 and 4).
157 Gene cluster 4, whose expression was highest in Oocysts 4, included functions related to the
158 cell cycle, with genes related to DNA replication and chromosome separation (Figure 1g,
159 Supplementary Table 4).

160 Finally, the fourth branch (gene clusters 3, 10, 14 and 15) was highly expressed in
161 Oocyst spz and characterized by clear signatures of sporozoite segmentation, including genes
162 involved in nuclear migration and proteins localizing to the inner membrane pellicle complex,
163 formed by the inner membrane complex (IMC), a scaffolding compartment essential for
164 daughter cell formation, and the cytoskeleton network supporting it, as well as the invasive
165 organelles, rhoptries, and micronemes [27, 28] (Figure 1g , Supplementary Table 4).

166 Although poly-A capture is not designed to target ribosomal RNAs (rRNAs), these
167 molecules are ubiquitously present in *Plasmodium* bulk and single cell RNA results [29]. We
168 detected limited expression of different rRNAs via random binding, organized in distinct gene
169 expression patterns (Supplementary Figure 3c). Expression of the A1/A2 forms that are
170 dominant in asexual parasites [30] appeared highest in ookinete clusters, then gradually
171 decreased—though not entirely to zero—in later stages. The two mosquito-stage rRNAs, S1

172 and S2 [30], were expressed throughout oocyst growth, with S1 (gene cluster 10) starting in
173 Took and S2 (gene cluster 13) in the d2 oocyst stage. These results add granularity to rRNA
174 expression during the *P. falciparum* life cycle [30].
175 Combined, these gene expression networks provide an unprecedented volume of
176 information on the key biological transitions occurring during parasite development in the
177 mosquito midgut, shedding light into the biology of these understudied stages.
178
179 ***Pf*ATP4 and *Pf*LRS regulate oocyst growth**
180 To assess the functional role of factors and pathways emerging from the gene network
181 analysis, we targeted candidates from the second and third branch that have known inhibitors
182 characterized in asexual blood stages. We first selected *Pf*ATP4, an Na^+-ATPase that is
183 essential for sodium ion efflux (second branch, gene cluster 5, Figure 2a) and is inhibited by
184 the drug cipargamin (CIP, original name: NITD609) [31]. We provided this drug to infected
185 female mosquitoes via sugar solution, from the onset of oocyst formation (2d pi) until 10d pi
186 (Figure 2b). While CIP did not reduce oocyst intensity or prevalence (Supplementary
187 Figure 4a), it considerably impaired oocyst growth to the extent that we did not detect any
188 sporozoites in the salivary glands at 14d pi, a time when sporozoites are abundant in control
189 mosquitoes (Figure 2c, d, Supplementary Figure 4b, c). Shorter exposure times (2-4d pi and
190 2-7d pi) also significantly reduced oocyst size and produced no sporozoites in the salivary
191 glands (Figure 2c, d, Supplementary Figure 4d). The severely reduced size and absence of
192 sporozoites after just 2 days of exposure suggest that regulation of sodium efflux is essential
193 during the early phases of oocyst growth.
194 We next targeted the leucine-tRNA ligase (*Pf*LRS**,** third branch, gene cluster 1,
195 Figure 2e), which can be inhibited by the compound MMV670325 (original name: AN6426) [32].
196 MMV670325 delivery in sugar between 2-10 d pi also impaired oocyst growth, albeit to a lesser
197 extent than CIP (Figure 2f, g), possibly due to the 200-fold higher IC_{50} of this compound in
198 blood stages [31]. MMV670325 treatment did not reduce oocyst prevalence, and induced a
199 slight, unexplained increase in infection intensity (Supplementary Figure 4e). Despite this
200 increase in oocyst numbers, the impact on growth led to significantly lower prevalence of
201 salivary gland sporozoites at 14d pi, resulting in 53% fewer females becoming infectious by
202 that time point (Figure 2h, pie charts).
203 These results highlight how knowledge of the processes affecting oocyst growth derived
204 from our scRNA-seq data can be utilized to identify targets to block parasite development in

205 the mosquito vector. Our findings align with previous studies using cytochrome b inhibitors [33]
206 and could potentially aid in the development of novel mosquito-based malaria control strategies
207 [34].
208
209 **_Pf_SIP2 ensures hepatocyte invasion**
210 In the final branch, along with rhoptry and cytoskeletal genes, we also detected an ApiAP2
211 transcription factor, *Pf*SIP2 (gene cluster 10) (Figure 1f, Figure 2i). *Pf*SIP2 is essential in
212 asexual blood stages, where it is implicated in heterochromatin formation [35], yet its function
213 during mosquito stages remains unknown. Based on its expression in late oocysts, we
214 reasoned that *Pf*SIP2 may play a role in sporozoite formation, invasion of salivary glands, or
215 sporozoite infectivity to liver cells. To test this hypothesis, we generated a conditional *Pf*SIP2
216 knockdown line integrating the TetR-DOZI aptamer system at the C-terminus (Supplementary
217 Figure 4f, g) [36]. Removal of anhydrotetracycline (ATc) in asexual blood stage cultures led to
218 parasite death, confirming the essentiality of *Pf*SIP2 (Supplementary Figure 4h) [35]. We
219 adapted the use of this system to mosquito stages by providing ATc throughout gametocyte
220 cultures and in the mosquitoes' daily sugar solutions, while gene knockdown was induced by
221 withdrawing the compound immediately before mosquito infection (Figure 2j). We did not
222 observe any difference between *Pf*SIP2 +ATc and –ATc groups in terms of oocyst intensity,
223 prevalence and size at 7d pi, and sporozoite intensity and prevalence at 14d pi, while *Pf*SIP2
224 parasites were less infectious to mosquitoes than wild type co-cultured ones, as often observed
225 in mosquito infections with transgenic parasites that have undergone bottlenecks during the
226 selection process (Supplementary Figure 4i-k). ATc withdrawal, however, severely impaired the
227 ability of *Pf*SIP2 sporozoites to invade primary human hepatocytes, inducing a remarkable
228 decrease in both invasion efficiency (67% reduction) and the formation of exoerythrocytic forms
229 (EEFs) (96% reduction) compared to *Pf*SIP2 parasites in the presence of ATc (Figure 2k-l).
230 As this transcription factor is not expressed in salivary gland sporozoites [37], our results
231 show that *Pf*SIP2 expression in late oocysts is essential for the ability of sporozoites to infect
232 hepatocytes, and the identification of its downstream targets could provide new candidates for
233 transmission blocking strategies.
234
235 **Parasite association with midgut cells**
236 Sequencing of both parasites and mosquito cells over time presented the opportunity to
237 identify possible interactions between the two organisms, as a parasite captured while either

238 inside a midgut cell or in strong association with one would share the same cellular barcode as
239 the mosquito cell. To identify these shared barcodes, defined here as dual-read cells, we first
240 built a single UMAP of midgut cells integrating data from all 4 time points in both ds*GFP* and
241 ds*EcR* mosquitoes, resulting in 18 clusters assigned to several mosquito cell types based on
242 marker genes (Figure 3a, Supplementary Figure 5a-d, Supplementary Table 5): progenitor
243 cells (i.e., intestinal stem cells/enteroblast, ISCs/EBs); posterior enterocytes (pECs); anterior
244 enterocytes (aECs); enteroendocrine cells (EEs); visceral muscles (VMs); and hemocyte and
245 fat body cells (HC/FB). Clusters with mixed markers were annotated as EC-like or EE-like.

246 As parasite numbers and expression profiles were very similar in ds*GFP* and ds*EcR*
247 females at 36h pi (Supplementary Figure 1b and 2a)— and a consistent lack of an immune
248 responses in these two groups of mosquitoes (Supplementary Figure 5e, Supplementary Table
249 6)— in subsequent analysis we combined the two parasite populations. Despite the fleeting
250 nature of midgut crossing [9, 10], we identified 147 dual-read cells out of the 1,017 parasites
251 sequenced at this time point (14.5%) (Figure 3b, Supplementary Figure 6a-b). This percentage
252 is significantly higher than the 4.3% observed at 2d pi (24 dual-read parasites out of 533 total,
253 Fisher exact test, p-value <0.001), when parasites have mostly transformed into oocysts.
254 Interestingly, dual-read parasites (ookinetes and tooks) appeared to interact preferentially with
255 the ISC/EB midgut cluster (Figure 3b-d). Indeed, 30% of dual-read cells included a progenitor
256 cell, although this cluster represents just 16.7% of all mosquito cells at this time point
257 (Figure 3d, OR 2.1, fdr = 0.036). This enrichment was not due to lower mRNA content in
258 ISC/EBs, which might artificially increase parasite mRNA detection rates (Supplementary
259 Figure 6c. We also observed that parasites were less likely to be associated with pECs than
260 expected by chance (Figure 3d , OR 0.47, fdr = 0.014). On the contrary, 2d pi dual-read
261 parasites showed no significant association with any particular mosquito cell type
262 (Supplementary Figure 6d).

263 To confirm these findings, we performed confocal microscopy using an anti-centrin
264 antibody that labels progenitor cells, as determined by their basal location, smaller triangular
265 shape, and colocalization with the known stem cell marker armadillo [38] (Supplementary
266 Figure 6e). We observed close interactions between parasites and progenitor cells, with 10.1%
267 of parasites (14 out of 138) appearing to be inside or in close contact with an ISC/EB (Figure 3e,
268 box 1-2), or oriented towards one (Supplementary Figure 6f). This number exceeds the 4.3%
269 observed by scRNA-seq, suggesting that the single cell isolation process had partially
270 preserved these interactions. Consistent with previous studies [10, 13, 39], we also observed

271 parasites near extruded pECs (Supplementary Figure 6f, Supplementary Video 1), as well as
272 pECs positive for the parasite protein Pfs25 (Supplementary Figure 6g). The reduced number
273 of dual-read pECs associated with parasites may therefore be explained by the extrusion of
274 some of these cells after ookinete traversal.
275 Combined, these data reveal a previously unrecognized preferential interaction between
276 parasites and mosquito progenitor cells during traversal of the midgut epithelium, before
277 ookinetes transform into oocysts.
278
279 **Late oocysts are associated with muscles**
280 When analyzing dual-read parasites at 7d pi, we were surprised to find that a large
281 proportion of oocysts (113 out of 410, 27.6%) shared a barcode with a mosquito cell, a
282 proportion significantly higher than at 4d pi (55 out of 1,535 parasites, 3.6%) (Supplementary
283 Figure 6a, Supplementary Figure 7a, b, Fisher exact test, p-value <0.001). This observation
284 suggests that the interaction progresses as the parasite develops and grows in size. Consistent
285 with this, the vast majority of these parasites were from the most mature oocyst clusters,
286 namely Oocyst 4 and Oocyst spz (97 out of 113, Figure 4a).
287 Remarkably, the vast majority (72%) of dual-read mosquito cells originated from the VM
288 cluster, which contains muscle cells surrounding the midgut epithelium (Fisher exact test, OR
289 25.6, p-value <0.001) (Figure 4b, c). Supporting this finding, we identified multiple instances of
290 phalloidin-stained visceral muscles closely wrapped around oocysts, with muscle fibers
291 extending beyond their usual width (Figure 4d, e; Supplementary Video 2). The presence of
292 both an oocyst – which is extracellular and on average above 25 μm in diameter at this time
293 point [18] – and a mosquito cell in the same droplet suggests a tight physical interaction
294 between the two.
295 We next explored whether dual-read VM cells showed a differential transcriptional profile
296 and detected significant upregulation of 24 genes (and a single downregulated gene) relative
297 to VM cells not in contact with a parasite (Supplementary Table 7). Interestingly, using
298 *Drosophila melanogaster* orthologs to assign function, we identified clear cell-cell adhesion
299 signals (Supplementary Figure 7c, Supplementary Table 7), suggesting that VM cells respond
300 to the presence of parasites by enhancing their adhesive properties.
301 These data demonstrate for the first time the occurrence of strong physical interactions
302 between late-stage oocysts and muscle cells, potentially tethering oocysts to the epithelial
303 layer.

304
305
306 **Discussion**

307 By providing valuable insight on developmental stages that had previously escaped large-
308 scale analysis, our study represents a momentous step towards a comprehensive
309 reconstruction of the events characterizing the *P. falciparum* transmission cycle. The rich
310 volume of information reported here significantly expands the repertoire of potential targets for
311 blocking parasite transmission by the *Anopheles* female in strategies based on transmission-
312 blocking drugs and vaccines [40] or mosquito-targeted antimalarials [34]. Indeed, our functional
313 analysis validates parasite factors (*Pf*ATP4, *Pf*LRS and *Pf*SIP2), essential for parasite growth
314 and acquisition of infectivity to human hepatocytes. We also identify changes in transcriptional
315 activity and RNA splicing, membrane and vesicle trafficking genes potentially involved in the
316 ookinete-oocyst transition, a possible role of *Pf*EMP1 in adherence of newly formed oocysts to
317 the midgut epithelium, and the progression of processes driving oocyst development, although
318 these findings will require validation in future studies. Excitingly, we identified cytoskeletal
319 components, such as the IMC, as well as multiple members of the basal complex and known
320 cell organizational machinery components [41], in oocysts that have begun sporozoite
321 segmentation. These results demonstrate that much of the core machinery necessary for
322 daughter cell production is conserved between blood stage parasites and oocysts, despite the
323 sheer difference in scale of this process between these stages.

324 The sequencing of both parasites and mosquito cells allowed the identification of
325 previously unappreciated interactions between the two organisms at the level of the midgut
326 epithelium. Several explanations may underlie the observed association of parasites with
327 midgut progenitor cells. Ookinete traversal of the midgut epithelium is an asynchronous
328 process that occurs between 24-36h pi. Recent studies suggest that the most plausible model
329 for midgut crossing involves ookinetes initially invading an epithelial cell, then moving laterally
330 to adjacent cells before reaching the basal side, often leading to the extrusion of the invaded
331 cells [4, 12, 42]. The observation that dual-read parasites contain not only ookinetes but also
332 transforming tooks suggests that this interaction with progenitor cells occurs not during the
333 initial invasion phase but as parasites reach the basal side, where they transition into oocysts.
334 While our findings merely scratch the surface of the mechanisms governing parasite exit and
335 ookinete transformation into oocysts, it is plausible that *P. falciparum* uses progenitor cells as
336 landmarks for reaching the basal side of the midgut. Here, parasite exit may be facilitated by

337 the remodelling of tight junctions during division of ISCs [43, 44], although several alternative
338 hypotheses are possible. These interactions likely occur after ookinetes have rapidly escaped
339 extruding pECs, as observed both in this study and in several others [12, 13, 39] and in
340 alignment with our observation of a slightly reduced number of parasite-associated pECs.
341 Interestingly, midgut progenitor cells were not observed to interact with ookinetes in the
342 rodent-infecting *P. berghei* model but were instead associated with late oocysts, where
343 progenitor expansion restricted oocyst growth and eventually led to parasite death [45]. In our
344 analyses, however, late *P. falciparum* oocysts did not interact with ISCs but were remarkably
345 associated with muscle cells. Such profound differences between *P. falciparum* and *P. berghei*
346 are not necessarily surprising, as they may be the result of the specific coevolutionary
347 trajectories of human malaria parasites with human-biting mosquitoes. Indeed, *P. falciparum*
348 has evolved mechanisms to minimize the damage inflicted to human-biting *Anopheles* vectors
349 during midgut traversal, including a tightly restricted number of ookinetes crossing the
350 epithelium [18, 46], whereas *P. berghei* and other mouse malaria parasites trigger substantial
351 fitness costs, likely due to the vast number of damaged pECs [47, 48]. Our observation of a
352 close association between late oocysts and mosquito VM cells is also consistent with a
353 scenario of reduced fitness costs caused by *P. falciparum*. Indeed, while *P. berghei* oocysts
354 become partially embedded in the epithelium, potentially inflicting damage that may trigger the
355 proliferation of ISCs [45], *P. falciparum* oocysts settle between the epithelium and basal lamina,
356 protruding further out and overall limiting their impact on midgut physiology [49]. Considering
357 the extensive thinning of the basal lamina as oocysts undergo their remarkable expansion [49,
358 50], tight interactions with muscle cells could be advantageous to the oocyst by allowing it to
359 remain tethered to the midgut while avoiding damage to the host. Further research will clarify
360 the biological relevance of the mosquito-parasite interactions we unveiled in this study.
361 Regardless of function, our data demonstrate that the *An. gambiae* midgut is the site of a
362 dynamic interplay with *P. falciparum* parasites, possibly evolved during the long co-existence
363 of these two organisms, and shaping the formidable transmission ability of these parasites.
364

365 **Acknowledgements**

366 The authors thank Rhoel Dinglasan and Marc-Jan Gubbels for insights on the centrin antibody,
367 and Jeffrey D. Dvorin for the tetR-DOZI and guide plasmids. We are grateful to Scott E. Lindner
368 for valuable discussions on rRNA, and to the members of the Catteruccia laboratory for their
369 suggestions and comments. We thank Lucia Ricci for help with graphics, and we acknowledge

370 Neha Damaraju for her assistance with hepatocyte infections. The armadillo monoclonal
371 antibody N2 7A1 developed by E. Wieschaus was obtained from the Developmental Studies
372 Hybridoma Bank, created by the NICHD of the NIH and maintained at The University of Iowa,
373 Department of Biology, Iowa City, IA 52242. We are deeply grateful to VeuPathDB for aiding
374 the analysis of the datasets. FC is funded by the Howard Hughes Medical Institute (HHMI) as
375 an HHMI Investigator and by the National Institute of Health (NIH) grants R01AI148646 and
376 R01AI153404. LEdV was funded by a Rubicon grant (452021309) from the Dutch Research
377 Council (NWO).
378

379 **Methods**

380

381 **Rearing of *An. gambiae* mosquitoes**

382 *Anopheles gambiae,* G3 strain mosquitoes were reared in an insectary maintained at 27°C, 70-
383 80% relative humidity, on a 12h: 12h light:dark cycle. Larvae were fed on fish food and adults
384 were provided with 10% w/v glucose solution *ad libitum*. Adult mosquitoes were fed with
385 purchased human blood (Research Blood Components, Boston, MA) to induce egg laying.

386

387 **dsRNA production and microinjection**

388 PCR fragments of *eGFP* control (495 bp) and *EcR* (AGAP029539; 435 bp) were amplified from
389 the plasmids pCR2.1-eGFP and pCR2.1-EcR as previously described [51]. PCR product was
390 used to transcribe dsRNA using the Megascript T7 transcription kit (Thermo Fisher Scientific),
391 per manufacturer's protocol. The resulting dsRNA was purified via phenol-chloroform and
392 diluted to a concentration of 10 µg/µL. Microinjections and resulting knockdown confirmation
393 were performed as detailed previously [18]. Briefly, adult mosquitoes were injected one day
394 post-eclosion and given an infectious blood meal 3 days post-injection.

395

396 **Culturing of *P. falciparum* NF54 parasites**

397 *P. falciparum* NF54 strain (BEI Resources, MRA-1000) was cultured as asexual stages at 37ºC
398 between 0.2 and 2% parasitemia in human erythrocytes at 5% hematocrit (Interstate Blood
399 Bank, Memphis TN) using RPMI medium 1640 supplemented with 25mM HEPES, 10mg/l
400 hypoxanthine, 0.2% sodium bicarbonate, and 10% heat-inactivated human serum (Interstate
401 Blood Bank) under a gas mixture of 5% O_2, 5% CO_2, balanced N_2. Stage V female and male
402 gametocytes were induced by raising parasitemia over 4% and incubating cultures for ~14–20
403 days with daily media change. Transgenic parasites were kept on 500 nM ATc in all cultures
404 unless specified.

405

406 ***P. falciparum* infections of *An. gambiae* mosquitoes**

407 Female mosquitoes were blood fed on a mix of *P. falciparum* gametocyte culture, human red
408 blood cells and human serum (ratio 1:3:6) via heated membrane feeders 3-5 days post
409 eclosion, and introduced into a custom-built glove box (Inert Technology, Amesbury MA) as
410 previously described [18]. In the case of transgenic parasites, ATc was washed from culture 1
411 hour before infection and either 500 nM ATc or DMSO were added to blood meal. Unfed

412 mosquitoes were removed and remaining mosquitoes were kept on 10% glucose solution *ad*
413 *libitum*, with added ATc or compound (see below). At dissection time points, mosquitoes were
414 aspirated into 80% ethanol, frozen for 10 minutes, and transferred to phosphate-buffered saline
415 (PBS) on ice.
416
417 **Post-infection exposure assays via sugar feeding**
418 Stock solutions of cipargamin (ChemPartner) and MMV670325 (Medicine for Malaria Venture)
419 were made in DMSO at 100 mM, preserved at -20°C and diluted 1:1,000 in 10% glucose
420 solution shortly before sugar change. ATc was dissolved directly in sugar solution to a final
421 concentration of 100 μM. Mosquito compound exposure through sugar feeding was performed
422 similarly as previously described [33]. Briefly, sugar solutions containing compounds or
423 corresponding controls (0.1% DMSO or 10% glucose only) were replaced every day. MMV325
424 and cipargamin exposure lasted from 2d to 10d pi (unless specified) while ATc was kept
425 throughout development in mosquito. For oocyst counts, midguts were collected at 7d pi and
426 stained in 2mM mercurochrome (Sigma-Aldrich, St. Louis, MO). Midguts were imaged using
427 an Olympus Inverted CKX41 microscope, and oocyst number and mean size were calculated
428 using OocystMeter [52]. For EcR knockdown confirmation, individual mosquito ovaries were
429 also collected in 80% ethanol for later counts. For salivary gland sporozoite quantification,
430 salivary glands of individual females were dissected at 14d pi in PBS and counted on a
431 hemocytometer.
432
433 **RNA extraction, cDNA synthesis and qRT-PCR**
434 Pools of 6-8 infected female mosquitoes were aspirated at 24h pi and transferred to TRI
435 reagent (Thermo Fisher Scientific). RNA was extracted, DNase treated, quantified, and reverse
436 transcribed as previously described [18]. cDNA from 4 biological replicates was diluted tenfold
437 and ran in duplicate for qRT-PCR as previously described [18]. Gene-specific primers were
438 used and relative quantification was performed with the ribosomal gene *Rpl19* as the reference
439 (Supplementary Table 8) [53]. RNA extraction from one replicate of the single-cell experiments
440 failed and were thus redone with samples collected at 2d pi.
441
442 **Generation of single-cell suspension**
443 Forty midguts from *P. falciparum*-infected mosquitoes injected with ds*GFP* or ds*EcR* were
444 dissected at 36h, 2d, 4d, and 7d pi in ice-cold PBS, and any remaining blood meal was

445 removed. Dissected midguts were stored in ice-cold, PBS for no longer than 1 hour to preserve
446 the viability of parasite and mosquito cells. Midguts were pooled into 200 µl of PBS with
447 1 mg/mL elastase (Sigma-Aldrich E7885) and 1 mg/mL collagenase IV (Thermo Fisher
448 Scientific 17104019), and incubated at 30ºC, 300 rpm for 30 mins in a shaking heat block. To
449 facilitate the isolation of single cells, samples were disrupted every 10 mins by pipetting. We
450 chose not to use fluorescence-activated or magnetic-activated cell sorting as they both
451 lengthen the isolation protocol and cause stress. Instead, the cell suspension was sequentially
452 passed through 70 µm, 40 µm, and 20 µm cell strainers (pluriSelect), with each strainer being
453 immediately washed with 200 µl of 1x PBS to collect any adherent cells. The 20 µm cell
454 strainers were not used for the 7d pi samples, as oocysts at this time point are, on average,
455 over 25 µm in diameter [18]. The final single-cell suspension was pelleted, resuspended in 20
456 µl of PBS, and cell concentration and viability was determined by hemocytometer count with
457 trypan blue.
458
459 **Single-cell library preparation and sequencing**
460 Targeted cell recovery was set to 4,000 cells, and single cells were loaded onto the 10X
461 chromium chip according to manufacturer's instructions. Chromium Next GEM Single Cell 3'
462 Reagents Kit v3.1 (Dual Index) was used and corresponding User Guide (RevC) followed.
463 Briefly, single cells were lysed in an emulsion, mRNA molecules were captured, and barcoded
464 cDNA were generated and amplified. cDNA quality and quantity of each sample were assessed
465 using the Agilent bioanalyzer and qPCR with i7 and i5 Illumina primers following protocol from
466 Universal Kapa Library Quantification Kit (Roche). The cDNA from each sample was then
467 mixed in equal proportions, spiked with 1% phage cDNA (PhiX, Illumina) and tested on the
468 Illumina iSeq 100 before being sequenced on two NovaSeq S4 flow cells for deep sequencing.
469
470 **scRNA-seq data processing**
471 For each sample, FASTQ files originating from different flow cells were concatenated and
472 mapped to the genomes of *P. falciparum* 3D7 (PlasmoDB.org, version 58) and *An. gambiae*
473 PEST (VectorBase.org, version 58) [54], respectively, using the 10X Cell Ranger software
474 v7.0.1 [55]. The resulting count matrix for each sample was processed and filtered using
475 Scanpy in Python (version 3.10) [56]. Based on the individual sample profile, low-quality cells,
476 dead cells, and empty droplets were removed according to the number of reads (UMI count),
477 number of genes (gene count), and, in the case of *P. falciparum*, the mitochondrial percentage

per cell (Supplementary table 1). The count matrix from each sample was merged into a single AnnData object by Scanpy, and doublets were removed running Scrublet software in Python before conversion to Seurat using SeuratDisk's function Convert.

scRNA-seq analysis of *P. falciparum*

Pseudobulk differential expression analyses were initially conducted treating the samples as independent observations for comparison. The pseudobulk count matrix was generated for each sample by summing raw gene counts across all cells in Python with Pegasus. Several comparisons were conducted – between each time point in parasites from ds*GFP*-injected mosquitoes as well as between parasites from ds*EcR*- and ds*GFP*-injected mosquitoes of the same time point – using a Python wrapper for the DESeq2 package from R [57]. Significance was set as $\log_2$ fold change greater than 1 or less than -1, and an adjusted p-value below 0.05. Functional enrichment analysis of upregulated or downregulated gene lists was performed using GoProfiler [58].

Standard single cell analysis pipeline was then performed with Seurat [59] and dependent packages in R 4.3.2 in RStudio 2023.9.1.494 [60]. Highly variable genes were identified with FindVariableFeatures function before data were scaled (ScaleData, default settings) and Principal Component Analysis plot was generated based on these features only. Next, high-quality parasite cells were integrated with existing datasets, including blood bolus ookinetes at 24h and 48h pi, gametes/zygotes/ookinetes from 2-20h pi, and sporozoites released from oocysts at 12d pi [15, 16]. Briefly, Seurat objects (v5) were created for external datasets and reads were normalized to 10,000 transcripts, before the three Seurat objects were merged. Variable features were identified with defaut parameters of FindVariableFeatures function, the data was scaled (ScaleData), and Principal component analysis (PCA) was performed on the first 50 dimensions (RunPCA, default settings). Integration was conducted using reciprocal PCA (RPCA), which is the preferred approach when minimal overlap between datasets is expected. Subsequently, a UMAP was generated including the top 12 principal components through the RunUMAP function, with parameters set to min.dist=0.4, and repulsion.strength=2. Cell clusters were defined by Louvain algorithm at a resolution of 0.5. Cluster markers were identified using the FindAllMarkers function, focusing only on positive markers with a log2 fold change above 1. Genes with false discovery rates below 0.01 were utilized to label each cluster. The Seurat object was converted into a cds object in Monocle3 [61], and the trajectory analysis was performed using the learn_graph function (close_loop = F, ncenter=500). Pseudotime

511 analysis was conducted by setting the node in the gamete/zygote cluster as the start point.
512 Gene network analysis focused on our data and was performed using the graph_test function
513 (neighbor_graph="principal_graph"), to identify co-expressed genes that change as a function
514 of pseudotime (FDR < 0.05). Co-expressed genes were further clustered by
515 find_gene_modules function with a resolution of 0.003. The expression of all genes within each
516 gene cluster was aggregated using the aggregate_gene_expression function. Enriched gene
517 ontology terms were determined by analyzing all the genes within a gene cluster in GoProfiler
518 [58].
519
520 **Plasmid construction**
521 The *Pf*SIP2 homology-directed repair (HDR) plasmid was assembled by golden gate cloning
522 (New England Biolabs) using purified PCR products of (1) a C-terminal homology region
523 (Cterm-HR) that was codon-altered to avoid repeated CRISPR cuts, (2) a cassette containing
524 hemagglutinin (HA)-tags, tet-aptamers [36], a TetR-DOZI fusion protein [36, 62], and a human
525 dihydrofolate reductase (hDHFR) selection marker, (3) a 3' HR, and (4) a bacterial backbone.
526 Primers used to amplify fragments are listed in Supplementary Table 8 and assembly was
527 confirmed by whole plasmid sequencing (Plasmidsaurus).
528 Two CRISPR-Cas9 guide plasmids were constructed to cut the C-terminus of the endogenous
529 *Pf*SIP2. Guide oligos were annealed and ligated into BpiI-digested pRR216 [63], which
530 contains *Sp*Cas9, a U6 guide cassette, and a yeast dihydroorotate dehydrogenase (DHODH)
531 selection marker. Sequences were confirmed by Sanger sequencing (Psomagen).
532
533 **Generation of PfSIP2-cKD line**
534 The HDR and guide plasmids of PfSIP2 were extracted using a Qiagen Maxi kit, and 100 µg of
535 the HDR plasmid was linearized with XhoI, NotI, and ApaL1 at 37ºC overnight. The linearized
536 HDR plasmid and a mixture of the 2 guide plasmids (60 µg each) were sterilized by ethanol
537 precipitation and resuspend in TE buffer.
538 The plasmids were then mixed with 270 µl of cytomix and transfection by red blood cell loading
539 was performed as described elsewhere [64]. The parasite line was maintained at 5% hematocrit
540 with 500 nM ATc (Sigma) from the onset of transfection. Drug pressure for the guide plasmid
541 was applied from 6 hours to 5 days post-transfection using 1.5 µM DSM1 (Sigma), whereas
542 drug pressure for the HDR plasmid was maintained with 2.5 nM WR99210 Hydrochloride
543 (Sigma) starting 6 hours post-transfection until integration was confirmed. To do so, genomic

544 DNA was extracted from WT and PfSIP2-cKD lines using the Qiagen Blood & Tissue kit. Each
545 integration site of the double crossover were amplified as well as the whole locus and PCR
546 products were analyzed by gel electrophoresis.
547
548 **Asexual stage growth assay**
549 ATc was washed from PfSIP2-cKD line three times with RPMI. The resulting parasites were
550 diluted to 0.5% starting parasitemia at 2.5% hematocrit and treated with either 500 nM ATc, 1.5
551 nM ATc, or 0.025% of DMSO. Parasitemia was calculated daily by counting Giemsa-stained
552 smears of each technical replicate. The experiment was repeated twice, with 4 technical
553 replicates for each biological replicate. Data were analyzed by two-way ANOVA with Dunn's
554 correction.
555
556 **Culturing of primary human hepatocytes and infection with transgenic parasites**
557 Cryopreserved human primary hepatocytes (BioIVT, Westbury, NY) were thawed, seeded on
558 collagen-coated micropatterned islands in 96 well plates, and infected with WT or *Pf*SIP2-cKD
559 sporozoites as previously described [65]. In short, WT or *Pf*SIP2-cKD-infected mosquito
560 salivary glands were dissected in Schneider medium (Gibco) containing 200 U/mL of penicillin
561 200µg/mL of streptomycin (2X, Gibco) for less than 1 hour. Sporozoites were released from
562 glands, filtered through a 35 µm cell strainer and counted on a hemocytometer. Parasites were
563 spun at 10,000 *g* for 3 min, resuspended in hepatocyte media containing 2.5 µg/mL Fungizone
564 (Cytiva) and 2X penicillin/streptomycin as well as either 500 nM ATc or 0.025% of DMSO and
565 seeded onto hepatocytes. For invasion assays, 7,000 sporozoites were seeded and wells were
566 fixed in 4% PFA 3h pi, followed by in/out CSP staining [65]. For infection assays, 70,000-
567 100,000 sporozoites were used, and subsequently washed off 3h pi before supporting cells
568 from the male mouse fibroblast cell line 3T3-J2 (Rheinwald and Green, 1975) were added.
569 Cells were washed daily, and wells were fixed 2d pi in 100% methanol and stained with mouse
570 αPfHSP70 monoclonal primary antibody (StressMarq SPC-186).
571
572 **Mosquito single cell analysis**
573 After quality control, mosquito cells from each time point were processed using a similar
574 workflow as for parasite analysis. The top 2,000 variable genes were identified, the data was
575 scaled, and PCA was performed computing the first 50 PCs. Integration was conducted using
576 RPCA to avoid overcorrecting for biological variation between time points. The UMAP was

577 calculated using the first 25 PCs, and cluster identification was based on the Louvain algorithm
578 with a resolution of 0.4. Positive markers were identified using the FindAllMarkers function with
579 a $\log_2$ fold change greater than 1. Clusters were annotated manually by cross-referencing
580 cluster markers from four references: the Fly Cell Atlas, the *Drosophila melanogaster* gut
581 single-cell study, the *Aedes aegypti* gut single-cell study, and the hemocyte single-cell study
582 from *An. gambiae* [66-69]. *An. gambiae* orthologs were identified using VectorBase [54], and
583 all significant cluster markers with an ortholog specific to a cell type were used for cluster
584 annotation.
585 Differential expression analysis comparing ds*EcR* and ds*GFP* injected mosquitoes at 36h pi
586 was performed by comparing both treatments binning for cell clusters to account for potential
587 differences in cell distribution (FindMarker). Comparison of visceral muscle (VM) cells with and
588 without dual-read parasites was done by selecting only VM cells at 7d pi and down sampling
589 non-dual-read VM cells to 150 cells to ensure a similar sample size before assessing gene
590 expression (FindMarker). *Drosophila melanogaster* orthologs were identified using VectorBase
591 [6] and used for the functional enrichment analysis as *An. gambiae* gene identifiers did not yield
592 any results. In both cases, the analysis was performed using GoProfiler [58].
593
594 **Immunofluorescent microscopy**
595 Midguts were dissected from females at specified time points. Any remaining blood bolus was
596 removed in ice-cold PBS when present and clean midguts were incubated at room temperature
597 in 4% paraformaldehyde (PFA) for 45 minutes, followed by 3 washes in PBS for 10 minutes
598 each. Midguts were permeabilized and blocked in 0.1% Triton X-100, 3% bovine serum albumin
599 (BSA) in PBS for 1 hour at room temperature or overnight at 4ºC before incubation in primary
600 antibody at room temperature for 2 hours, shaking. The following primary antibodies were used:
601 1:200 anti-*Toxoplasma gondii* centrin-1 rabbit polyclonal (Kerafast EBC004); 1:5 anti-
602 *Drosophila* armadillo mouse monoclonal supernatant N2 7A1 [70] (deposited to the DSHB by
603 E. Weischaus), 1:200 anti-Pfs25 mouse monoclonal 4B7 [71] (deposited to BEI resources by
604 Louis H. Miller and Allan Saul). Another 3 washes in PBS were performed before incubating
605 the samples in secondary antibodies and phalloidin (as required) for 1 hour at room
606 temperature rocking (goat anti-rabbit IgG AlexaFluor 488, goat anti-mouse IgG AlexaFluor 488,
607 goat anti-mouse AlexaFluor 568 from Invitrogen used at 1:400, Ebioscience Phalloidin eFluor
608 660 used 1:300). Midguts were then stained in PBS containing 5 µg/mL DAPI before the
609 remaining 3 washes in PBS only. Midguts were mounted using VECTASHIELD HardSet

610 Antifade Mounting Medium and imaged on a Zeiss Inverted Observer Z1 with Apotome3 or a
611 Zeiss LSM 980 confocal microscope. Confocal images were processed with LSMPlus on ZEN
612 3.10, followed by brightness and contrast adjustments in Fiji (version 2.14.0) [72]. Gamma was
613 left untouched unless specified.
614
615 **Statistical analysis**
616 Specific statistical tests are detailed in the corresponding figure legend. Confirmation of EcR
617 knockdown and analysis of parasite prevalence, intensity and infection rates were done using
618 GraphPad Prism 10.1.1. Odds ratio of dual-read parasites in mosquito cell types were
619 calculated in R using Fisher's exact test and correcting for multiple comparisons with
620 Benjamini-Hochberg.
621

References

1. *World malaria report 2023*. 2023, World Health Organization: Geneva.
2. Vlachou, D., et al., *The developmental migration of Plasmodium in mosquitoes.* Curr Opin Genet Dev, 2006. **16**(4): p. 384-91.
3. Smith, R.C., J. Vega-Rodriguez, and M. Jacobs-Lorena, *The Plasmodium bottleneck: malaria parasite losses in the mosquito vector.* Mem Inst Oswaldo Cruz, 2014. **109**(5): p. 644-61.
4. Carter, V., et al., *Minimum requirements for ookinete to oocyst transformation in Plasmodium.* Int J Parasitol, 2007. **37**(11): p. 1221-32.
5. Hentzschel, F. and F. Frischknecht, *Still enigmatic: Plasmodium oocysts 125 years after their discovery.* Trends Parasitol, 2022. **38**(8): p. 610-613.
6. Howick, V.M., et al., *The Malaria Cell Atlas: Single parasite transcriptomes across the complete Plasmodium life cycle.* Science, 2019. **365**(6455).
7. Afriat, A., et al., *A spatiotemporally resolved single-cell atlas of the Plasmodium liver stage.* Nature, 2022. **611**(7936): p. 563-569.
8. Modrzynska, K., et al., *A Knockout Screen of ApiAP2 Genes Reveals Networks of Interacting Transcriptional Regulators Controlling the Plasmodium Life Cycle.* Cell Host Microbe, 2017. **21**(1): p. 11-22.
9. Zieler, H. and J.A. Dvorak, *Invasion in vitro of mosquito midgut cells by the malaria parasite proceeds by a conserved mechanism and results in death of the invaded midgut cells.* Proc Natl Acad Sci U S A, 2000. **97**(21): p. 11516-21.
10. Trisnadi, N. and C. Barillas-Mury, *Live In Vivo Imaging of Plasmodium Invasion of the Mosquito Midgut.* mSphere, 2020. **5**(5).
11. Volohonsky, G., et al., *Kinetics of Plasmodium midgut invasion in Anopheles mosquitoes.* PLoS Pathog, 2020. **16**(9): p. e1008739.
12. Baton, L.A. and L.C. Ranford-Cartwright, *How do malaria ookinetes cross the mosquito midgut wall?* Trends Parasitol, 2005. **21**(1): p. 22-8.
13. Han, Y.S., et al., *Molecular interactions between Anopheles stephensi midgut cells and Plasmodium berghei: the time bomb theory of ookinete invasion of mosquitoes.* EMBO J, 2000. **19**(22): p. 6030-40.
14. Zhang, M., et al., *Uncovering the essential genes of the human malaria parasite Plasmodium falciparum by saturation mutagenesis.* Science, 2018. **360**(6388).
15. Real, E., et al., *A single-cell atlas of Plasmodium falciparum transmission through the mosquito.* Nat Commun, 2021. **12**(1): p. 3196.
16. Mohammed, M., et al., *Single-Cell Transcriptomics To Define Plasmodium falciparum Stage Transition in the Mosquito Midgut.* Microbiol Spectr, 2023. **11**(2): p. e0367122.
17. Graumans, W., et al., *When Is a Plasmodium-Infected Mosquito an Infectious Mosquito?* Trends Parasitol, 2020. **36**(8): p. 705-716.
18. Werling, K., et al., *Steroid Hormone Function Controls Non-competitive Plasmodium Development in Anopheles.* Cell, 2019. **177**(2): p. 315-325 e14.
19. Redfern, C.P.F., *20-Hydroxy-ecdysone and ovarian development in Anopheles stephensi.* Journal of Insect Physiology, 1982. **28**(2): p. 97-109.
20. Werling, K., et al., *Development of circulating isolates of Plasmodium falciparum is accelerated in Anopheles vectors with reduced reproductive output.* PLoS Negl Trop Dis, 2024. **18**(1): p. e0011890.
21. Frischknecht, F. and K. Matuschewski, *Plasmodium Sporozoite Biology.* Cold Spring Harb Perspect Med, 2017. **7**(5).

670 22. Fernandes, P., et al., *The AMA1-RON complex drives Plasmodium sporozoite invasion*
671 *in the mosquito and mammalian hosts.* PLoS Pathog, 2022. **18**(6): p. e1010643.
672 23. Zeeshan, M., et al., *Plasmodium ARK2 and EB1 drive unconventional spindle*
673 *dynamics, during chromosome segregation in sexual transmission stages.* Nat
674 Commun, 2023. **14**(1): p. 5652.
675 24. Tsai, Y.L., et al., *Disruption of Plasmodium falciparum chitinase markedly impairs*
676 *parasite invasion of mosquito midgut.* Infect Immun, 2001. **69**(6): p. 4048-54.
677 25. Ecker, A., et al., *Reverse genetics screen identifies six proteins important for malaria*
678 *development in the mosquito.* Mol Microbiol, 2008. **70**(1): p. 209-20.
679 26. Deitsch, K.W. and R. Dzikowski, *Variant Gene Expression and Antigenic Variation by*
680 *Malaria Parasites.* Annu Rev Microbiol, 2017. **71**: p. 625-641.
681 27. Ferreira, J.L., et al., *The Dynamic Roles of the Inner Membrane Complex in the*
682 *Multiple Stages of the Malaria Parasite.* Front Cell Infect Microbiol, 2020. **10**: p.
683 611801.
684 28. Liffner, B., et al., *The Ins and Outs of Plasmodium Rhoptries, Focusing on the*
685 *Cytosolic Side.* Trends Parasitol, 2021. **37**(7): p. 638-650.
686 29. Bogale, H.N., et al., *Transcriptional heterogeneity and tightly regulated changes in*
687 *gene expression during Plasmodium berghei sporozoite development.* Proc Natl Acad
688 Sci U S A, 2021. **118**(10).
689 30. McGee, J.P., J.P. Armache, and S.E. Lindner, *Ribosome heterogeneity and*
690 *specialization of Plasmodium parasites.* PLoS Pathog, 2023. **19**(4): p. e1011267.
691 31. Spillman, N.J., et al., *Na(+) regulation in the malaria parasite Plasmodium falciparum*
692 *involves the cation ATPase PfATP4 and is a target of the spiroindolone antimalarials.*
693 Cell Host Microbe, 2013. **13**(2): p. 227-37.
694 32. Sonoiki, E., et al., *Antimalarial Benzoxaboroles Target Plasmodium falciparum Leucyl-*
695 *tRNA Synthetase.* Antimicrob Agents Chemother, 2016. **60**(8): p. 4886-95.
696 33. Paton, D.G., et al., *Using an antimalarial in mosquitoes overcomes Anopheles and*
697 *Plasmodium resistance to malaria control strategies.* PLoS Pathog, 2022. **18**(6): p.
698 e1010609.
699 34. Paton, D.G., et al., *Exposing Anopheles mosquitoes to antimalarials blocks*
700 *Plasmodium parasite transmission.* Nature, 2019. **567**(7747): p. 239-243.
701 35. Flueck, C., et al., *A major role for the Plasmodium falciparum ApiAP2 protein PfSIP2 in*
702 *chromosome end biology.* PLoS Pathog, 2010. **6**(2): p. e1000784.
703 36. Rajaram, K., H.B. Liu, and S.T. Prigge, *Redesigned TetR-Aptamer System To Control*
704 *Gene Expression in Plasmodium falciparum.* mSphere, 2020. **5**(4).
705 37. Lindner, S.E., et al., *Transcriptomics and proteomics reveal two waves of translational*
706 *repression during the maturation of malaria parasite sporozoites.* Nat Commun, 2019.
707 **10**(1): p. 4964.
708 38. Ohlstein, B. and A. Spradling, *The adult Drosophila posterior midgut is maintained by*
709 *pluripotent stem cells.* Nature, 2006. **439**(7075): p. 470-4.
710 39. Baton, L.A. and L.C. Ranford-Cartwright, *Plasmodium falciparum ookinete invasion of*
711 *the midgut epithelium of Anopheles stephensi is consistent with the Time Bomb model.*
712 Parasitology, 2004. **129**(Pt 6): p. 663-76.
713 40. Miura, K., et al., *Vaccines and monoclonal antibodies: new tools for malaria control.*
714 Clin Microbiol Rev, 2024. **37**(2): p. e0007123.
715 41. Rudlaff, R.M., et al., *An essential contractile ring protein controls cell division in*
716 *Plasmodium falciparum.* Nat Commun, 2019. **10**(1): p. 2181.

42. Alves, E.S.T.L., et al., *The heat shock protein Hsc70-3 mediates an anti-apoptotic response critical for Plasmodium evasion of Anopheles gambiae immunity.* Microbiol Spectr, 2023. **11**(6): p. e0094023.
43. Resnik-Docampo, M., et al., *Tricellular junctions regulate intestinal stem cell behaviour to maintain homeostasis.* Nat Cell Biol, 2017. **19**(1): p. 52-59.
44. Pearce, S.C., et al., *Marked differences in tight junction composition and macromolecular permeability among different intestinal cell types.* BMC Biol, 2018. **16**(1): p. 19.
45. Barletta, A.F., et al., *Mosquito midgut stem cell cellular defense response limits Plasmodium parasite infection.* Nat Commun, 2024. **15**(1): p. 1422.
46. Marcenac, P., et al., *A mating-induced reproductive gene promotes Anopheles tolerance to Plasmodium falciparum infection.* PLoS Pathog, 2020. **16**(12): p. e1008908.
47. Almeida, A.P. and P.F. Billingsley, *Induced immunity against the mosquito Anopheles stephensi (Diptera: Culicidae): effects of cell fraction antigens on survival, fecundity, and plasmodium berghei (Eucoccidiida: Plasmodiidae) transmission.* J Med Entomol, 2002. **39**(1): p. 207-14.
48. Ahmed, A.M., et al., *Effects of malaria infection on vitellogenesis in Anopheles gambiae during two gonotrophic cycles.* Insect Mol Biol, 2001. **10**(4): p. 347-56.
49. Meis, J.F., et al., *A scanning electron microscopic study of the sporogonic development of Plasmodium falciparum in Anopheles stephensi.* Acta Trop, 1992. **50**(3): p. 227-36.
50. Sinden, R.E. and K. Strong, *An ultrastructural study of the sporogonic development of Plasmodium falciparum in Anopheles gambiae.* Trans R Soc Trop Med Hyg, 1978. **72**(5): p. 477-91.
51. Baldini, F., et al., *The interaction between a sexually transferred steroid hormone and a female protein regulates oogenesis in the malaria mosquito Anopheles gambiae.* PLoS Biol, 2013. **11**(10): p. e1001695.
52. Peng, D., Marrogi, E., Nelson, E., Liu, Q., Rinvee, T., DeVries, L., Singh, N., Shaw, R., Catteruccia, F., *OocystMeter: accurate segmentation of Plasmodium oocysts in mercurochrome-stained Anopheles mosquito midgut images (1.0.0)*. 2024, Zenodo.
53. Livak, K.J. and T.D. Schmittgen, *Analysis of relative gene expression data using real-time quantitative PCR and the 2(-Delta Delta C(T)) Method.* Methods, 2001. **25**(4): p. 402-8.
54. Alvarez-Jarreta, J., et al., *VEuPathDB: the eukaryotic pathogen, vector and host bioinformatics resource center in 2023.* Nucleic Acids Res, 2024. **52**(D1): p. D808-D816.
55. Zheng, G.X., et al., *Massively parallel digital transcriptional profiling of single cells.* Nat Commun, 2017. **8**: p. 14049.
56. Wolf, F.A., P. Angerer, and F.J. Theis, *SCANPY: large-scale single-cell gene expression data analysis.* Genome Biol, 2018. **19**(1): p. 15.
57. Love, M.I., W. Huber, and S. Anders, *Moderated estimation of fold change and dispersion for RNA-seq data with DESeq2.* Genome Biol, 2014. **15**(12): p. 550.
58. Kolberg, L., et al., *g:Profiler-interoperable web service for functional enrichment analysis and gene identifier mapping (2023 update).* Nucleic Acids Res, 2023. **51**(W1): p. W207-W212.
59. Stuart, T., et al., *Comprehensive Integration of Single-Cell Data.* Cell, 2019. **177**(7): p. 1888-1902 e21.

60. Team, R.C., *R: A Language and Environment for Statistical Computing*. 2023: Vienna, Austria.
61. Cao, J., et al., *The single-cell transcriptional landscape of mammalian organogenesis.* Nature, 2019. **566**(7745): p. 496-502.
62. Ganesan, S.M., et al., *Synthetic RNA-protein modules integrated with native translation mechanisms to control gene expression in malaria parasites.* Nat Commun, 2016. **7**: p. 10727.
63. Cepeda Diaz, A.K., et al., *Essential function of alveolin PfIMC1g in the Plasmodium falciparum asexual blood stage.* mBio, 2023. **14**(5): p. e0150723.
64. Deitsch, K., C. Driskill, and T. Wellems, *Transformation of malaria parasites by the spontaneous uptake and expression of DNA from human erythrocytes.* Nucleic Acids Res, 2001. **29**(3): p. 850-3.
65. March, S., et al., *Autonomous circadian rhythms in the human hepatocyte regulate hepatic drug metabolism and inflammatory responses.* Sci Adv, 2024. **10**(17): p. eadm9281.
66. Cui, Y. and A.W.E. Franz, *Heterogeneity of midgut cells and their differential responses to blood meal ingestion by the mosquito, Aedes aegypti.* Insect Biochem Mol Biol, 2020. **127**: p. 103496.
67. Raddi, G., et al., *Mosquito cellular immunity at single-cell resolution.* Science, 2020. **369**(6507): p. 1128-1132.
68. Hung, R.J., et al., *A cell atlas of the adult Drosophila midgut.* Proc Natl Acad Sci U S A, 2020. **117**(3): p. 1514-1523.
69. Li, H., et al., *Fly Cell Atlas: A single-nucleus transcriptomic atlas of the adult fruit fly.* Science, 2022. **375**(6584): p. eabk2432.
70. Riggleman, B., P. Schedl, and E. Wieschaus, *Spatial expression of the Drosophila segment polarity gene armadillo is posttranscriptionally regulated by wingless.* Cell, 1990. **63**(3): p. 549-60.
71. Barr, P.J., et al., *Recombinant Pfs25 protein of Plasmodium falciparum elicits malaria transmission-blocking immunity in experimental animals.* J Exp Med, 1991. **174**(5): p. 1203-8.
72. Schindelin, J., et. al, *Fiji: an open-source platform for biological-image analysis*. Nature Methods, 2012. **9**(7), p. 676–682

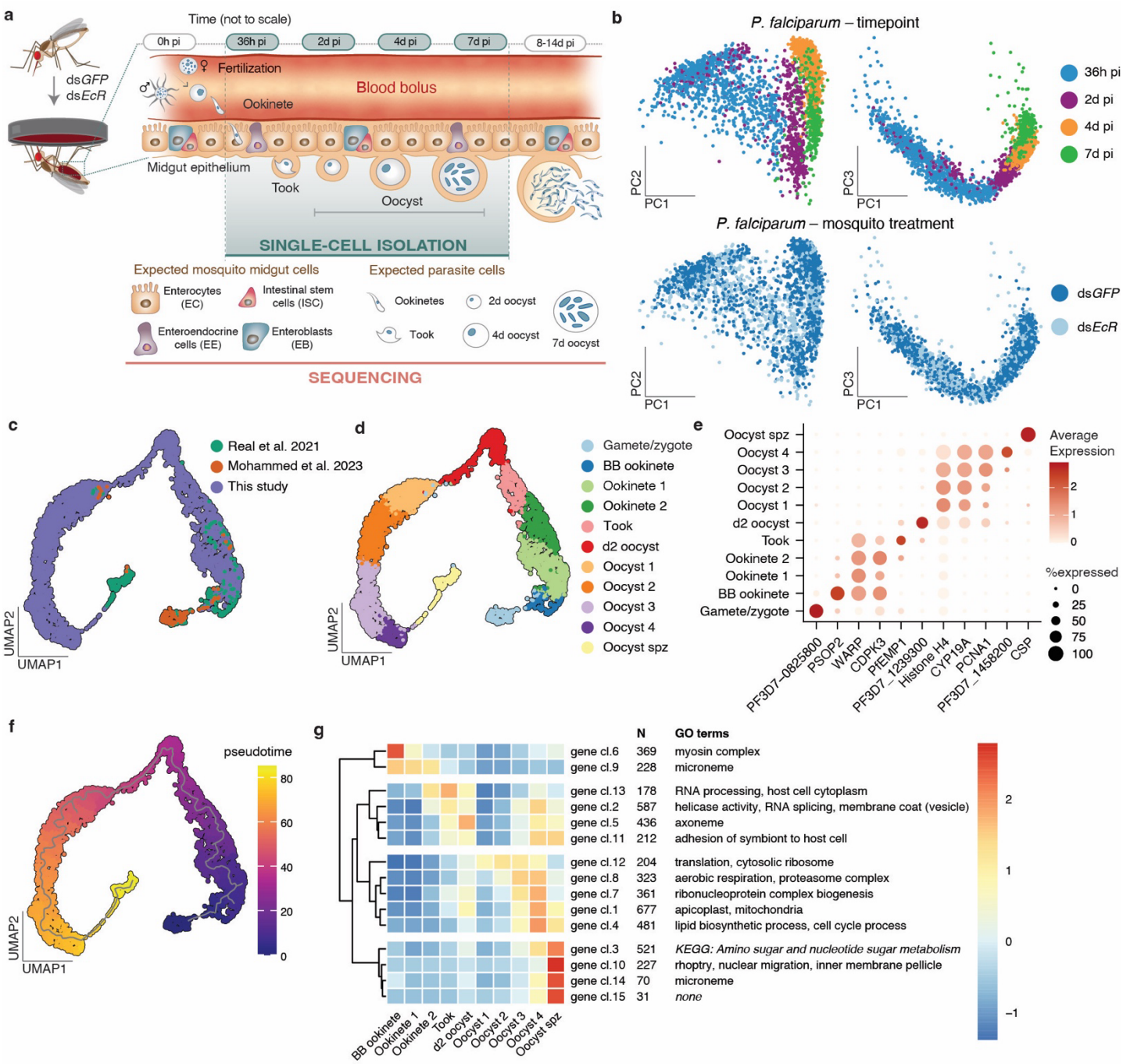

Figure 1 | Single cell RNA-seq provides a complete map of *P. falciparum* midgut stages

a, Schematic of dual single-cell RNA sequencing (dual scRNA-seq) displaying expected parasite forms and mosquito midgut cell types. Single *P. falciparum* parasites and *An. gambiae* midgut cells were collected from GFP (control) and EcR-depleted mosquitoes at the time points indicated by the shaded area: 36h post infection (h pi), 2 days post infection (d pi), 4d pi, and 7d pi. **b,** PCA plots of the 3,495 parasites collected across the four timepoints (top) and the two treatments (bottom). **c-d,** UMAP plots (**c**) integrating our scRNA-seq data with midgut stage data from two other studies [15, 16], and (**d**) showing 11 distinct parasite clusters. **e,** Dot plot of the best marker genes for each of the parasite clusters, showing their normalized average expression (color) and the proportion of parasites expressing each gene (size). **f,** Pseudotime analysis of the integrated scRNA-seq data. **g,** Gene\ cluster analysis of our expression data identifies four main branches of co-expressed genes across the different clusters (gene cl: gene cluster, N: number of genes in the cluster). Selected GO terms and KEGG annotations enriched in each gene cluster are indicated whenever present.

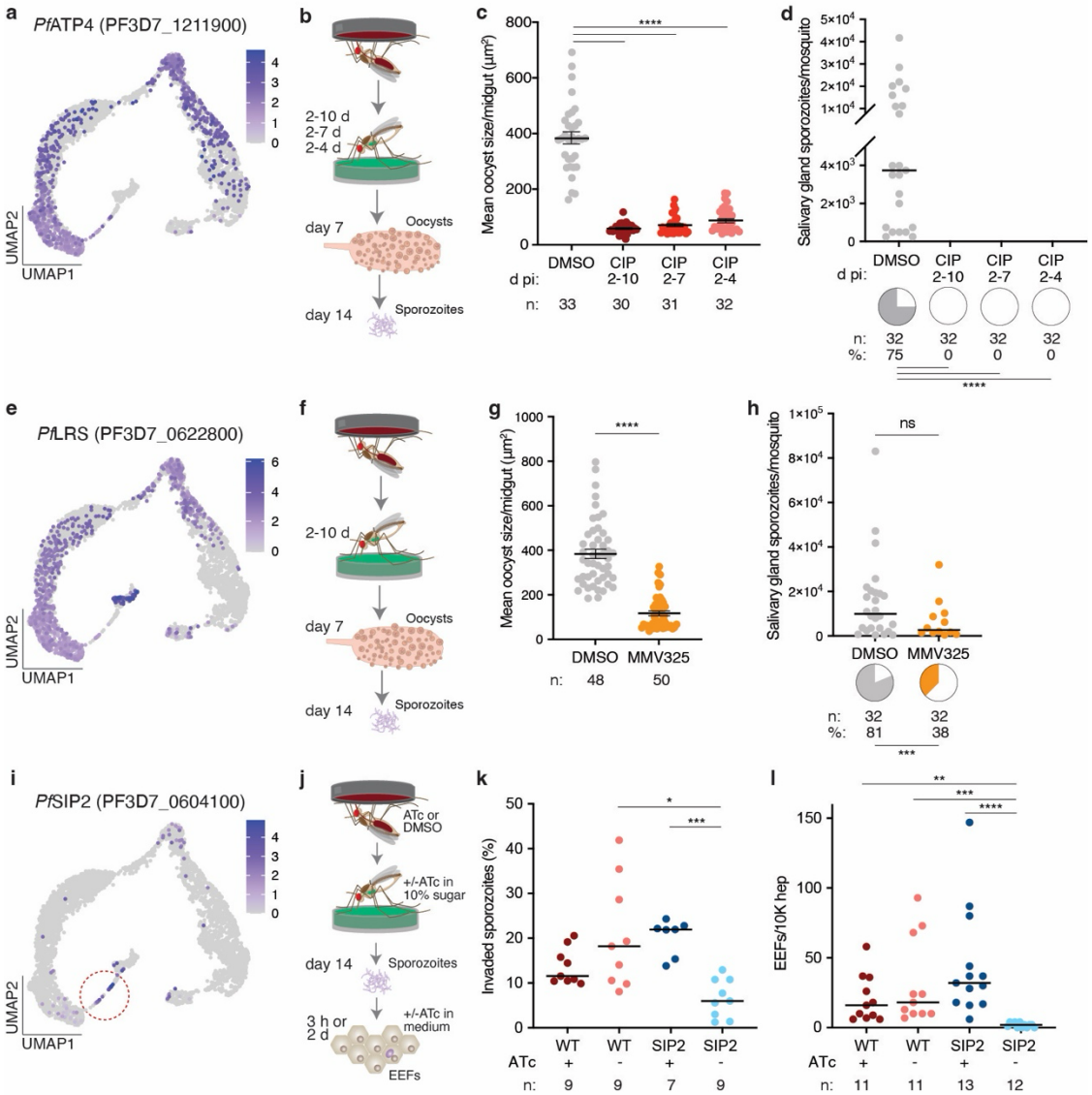

Figure 2 | Functional analysis of candidate genes from the gene network

a, Expression profile of *Pf*ATP4 (PF3D7_1211900), the target of cipargamin (CIP). **b-d,** CIP exposure (**b**) via sugar solution at 100 µM delivered for three different durations post-blood feeding (**c**) reduced oocyst size at 7d pi (one-way ANOVA, Dunn's correction), subsequently leading to (**d**) no sporozoites in the salivary glands at 14d pi (pairwise two-sided chi-squared test). Pie charts indicate infection prevalence. **e,** Expression profile of *Pf*LRS (PF3D7_0622800), the target of MMV670325 (MMV325). **f-h,** MMV325 exposure (**f**) at 100 µM via sugar solution from 2-10d pi (**g**) impaired oocyst size at d7 pi (t-test, two-tailed) and (**h**) reduced sporozoite prevalence (pie charts, Fisher's exact test, two-tailed) but not intensity (Mann-Whitney test, two-tailed) in salivary glands at 14d pi. **i,** Expression of *Pf*SIP2 (PF3D7_0604100) is highest in sporozoites within segmenting oocysts (circled in the UMAP). **j-l,** (**j**) Schematic representation of primary human hepatocyte infections with *Pf*SIP2 knockdown parasites. (**k**) Knockdown by ATc (500 nM) withdrawal impaired sporozoite invasion of primary hepatocytes at 3h pi (Kruskal-Wallis test, Dunn's correction) and (**l**) reduced extra erythrocytic forms (EEF) formation at 2d pi (Kruskal-Wallis test, Dunn's correction). Data are represented as mean ± SEM in panels **c** and **g**, and as median in panels **d, h, k** and **l**. *n* indicates the number of mosquito samples pooled from three independent infections (two for *Pf*LRS) in panels **c, d, g,** and **h,** or the number of independent wells in panels **k** and **l**. *p < 0.05, **p < 0.01, ***p < 0.001, ****p < 0.0001.

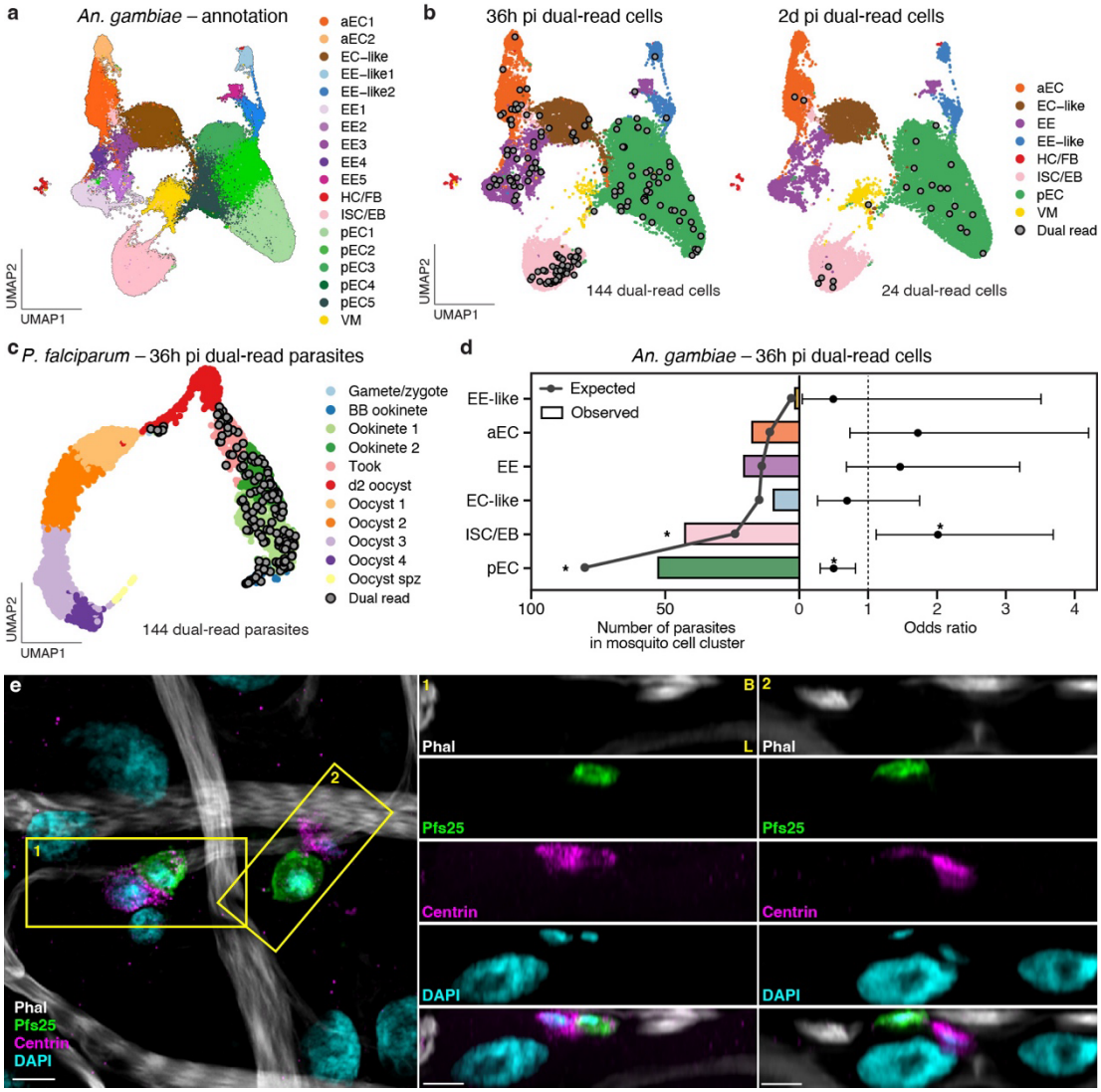

Figure 3 | Parasite interactions with progenitor cells during midgut traversal

a, UMAP of *An. gambiae* midgut cells across all 4 time points forms 18 cell clusters, representing different cell types: anterior enterocytes (aECs), enteroendocrine cells (EEs), hemocyte and fat body cells (HC/FB), intestinal stem cells/enteroblast, (ISCs/EBs), posterior enterocytes (pECs) and visceral muscles (VMs) as well as 3 clusters with mixed markers annotated EC-like or EE-like. **b,** UMAP plots of *An. gambiae* colored by cell type and overlaid with dual-read cells (cells with both a mosquito and parasite barcode)(grey circles) at 36h pi (left) and 2d pi (right). **c,** UMAP plot of *P. falciparum* from this study overlaid with dual-read parasites (grey circles) at 36h pi. **d,** Statistical analysis of the distribution of dual-read parasites in mosquito cell types at 36h pi with the observed vs. expected numbers under the random distribution (left x axis) and resulting odds ratio (right x axis) (Fisher's exact test, *: false discovery rate < 0.05). **e**, Confocal imaging shows some parasites are inside of, or interact with, progenitor cells at 36h pi. Maximum intensity projection of a 9.66 µm Z-stack (0.21 µm between each plane) showing interactions between parasites (Pfs25, green) and progenitor cells (Centrin, magenta) (left image). Two orthogonal slices (yellow boxes) show parasites possibly inside (box 1) and adjacent (box 2) to progenitor cells. Nuclei were stained with DAPI (cyan), and muscle actin with phalloidin (Phal, white). LSM Plus processing was used. Scale bar: 5 µm. **All panels**, see main text for abbreviations.

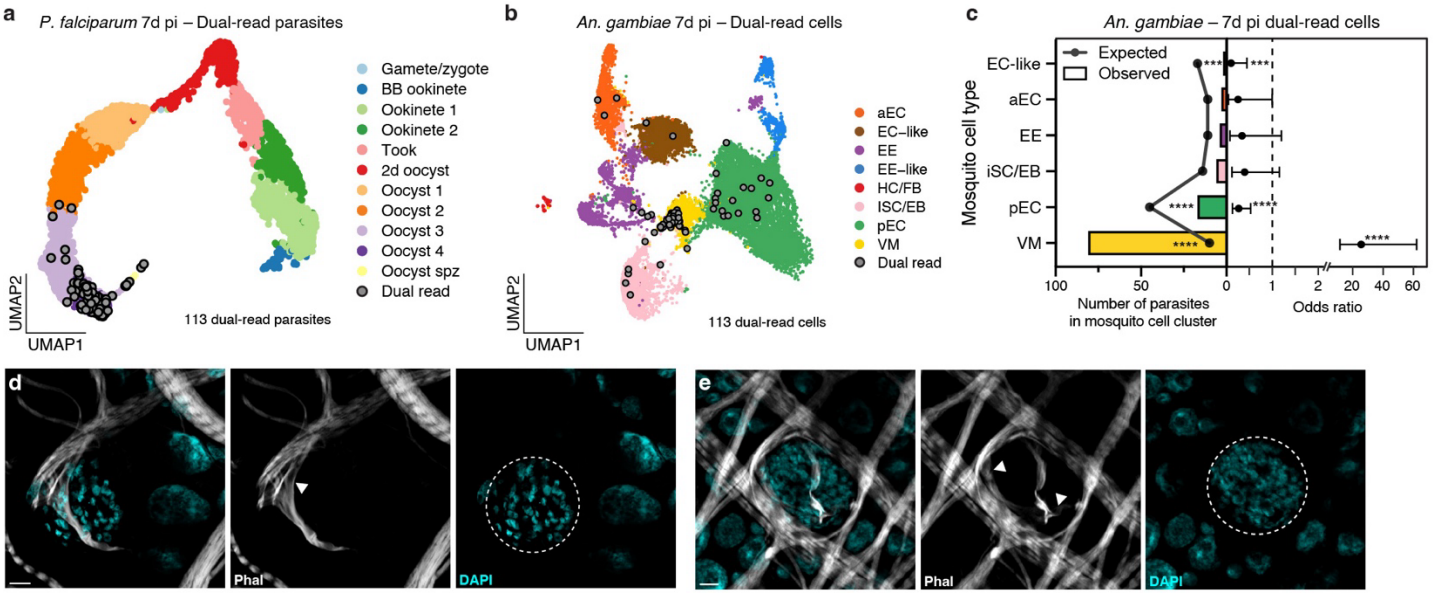

Figure 4 | Late oocysts interact with visceral muscles

a-b, UMAPs of 7d pi dual-read (**a**) *P. falciparum* parasites and (**b**) *An. gambiae* midgut cells. **c,** Statistical analysis of the distribution of dual-read parasites in mosquito cell types at 7d pi with the observed vs. expected numbers under the random distribution (left x axis) and resulting odds ratio (right x axis) (Fisher's exact test, ***: fdr < 0.001, **** fdr < 0.0001). **d-e**, Maximum intensity projection of a 16.8 µm Z-stack of oocysts and muscle fibers at 7d pi, showing (**d**) muscle fibers forcefully stretched (arrowhead) around a large oocyst (dotted white line) or (**e**) encasing an oocyst. Nuclei were stained with DAPI (cyan) and muscle actin with phalloidin (Phal, white). Scale bar: 5 µm.

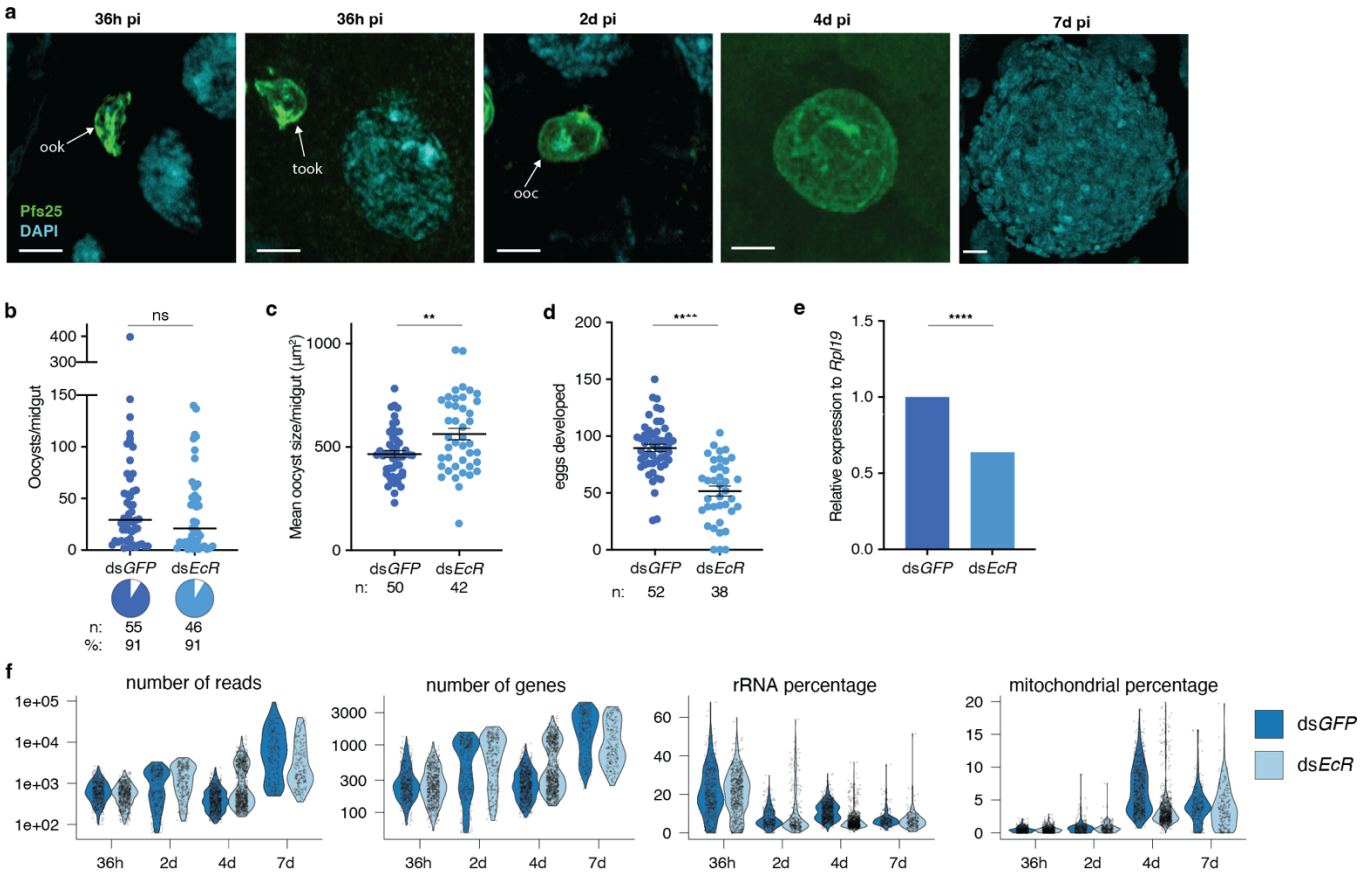

Supplementary Figure 1 | Quality control (QC) of scRNA-seq in two metabolic conditions
a, Representative images of the parasite forms collected during the 4 experimental time points. Ookinetes and tooks found at 36h pi, and oocysts identified at 2d, 4d, and 7d pi. Parasites were stained with Pfs25 (green) and nuclei with DAPI (cyan). Scale bar: 5 µm. **b, c**, *EcR* knockdown across 4 replicates (**b**) did not affect oocyst prevalence (pie-charts, Fisher's exact test, two-tailed) or intensity (Mann-Whitney test, two-tailed), but (**c**) increased oocyst size at 7d pi (unpaired t-test, two-tailed). **d-e**, Knockdown of *EcR* was confirmed by (**d**) detecting the expected reduction in egg numbers in the ovaries (unpaired t-test, two-tailed) and (**e**) RT-qPCR (unpaired t-test, two-tailed). **f**, Violin plots displaying key metrics of the *P. falciparum* scRNA-seq data after QC. *n* indicates the number of mosquitoes.

a

Comparison	number of upregulated genes	number of downregulated genes
GFP 2d vs GFP 36h	666	604
GFP 4d vs GFP 2d	345	619
GFP 7d vs GFP 4d	36	84
EcR 36h vs GFP 36h	0	0
EcR 2d vs GFP 2d	0	0
EcR 4d vs GFP 4d	0	0
EcR 7d vs GFP 7d	63	0

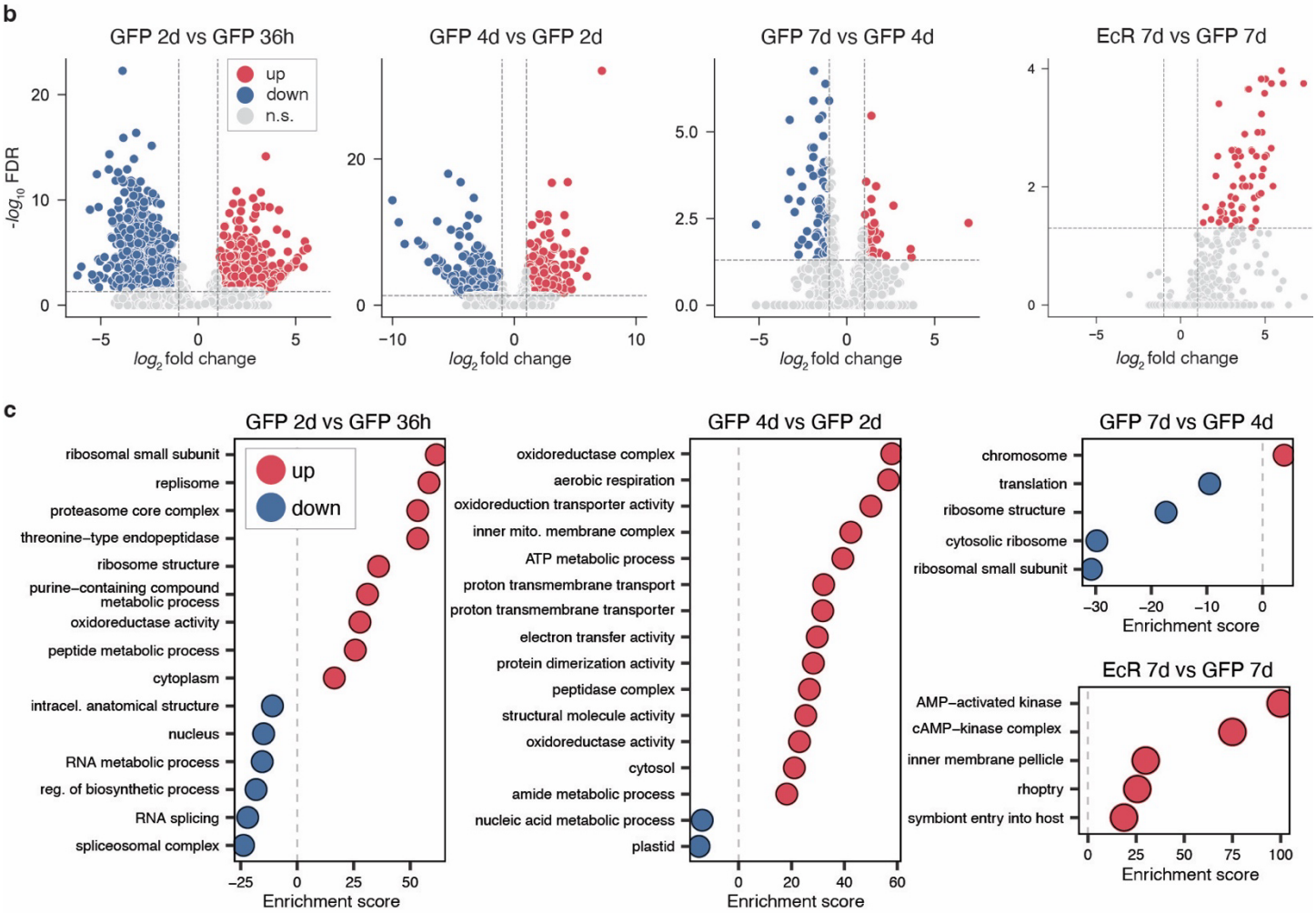

Supplementary Figure 2 | Pseudobulk differential expression analysis of *P. falciparum* across time and treatment

a, Table summarizing the number of up- and down-regulated genes identified in the comparisons of timepoints and/or treatments by pseudobulk (significance defined as FDR < 0.05 and absolute value of $\log_2$ fold change > 1). **b**, Volcano plots representing the differentially regulated genes in the four comparisons that yield significant changes. **c**, Corresponding GO terms that are significantly enriched in up- and down-regulated genes (Fisher's one-tailed test).

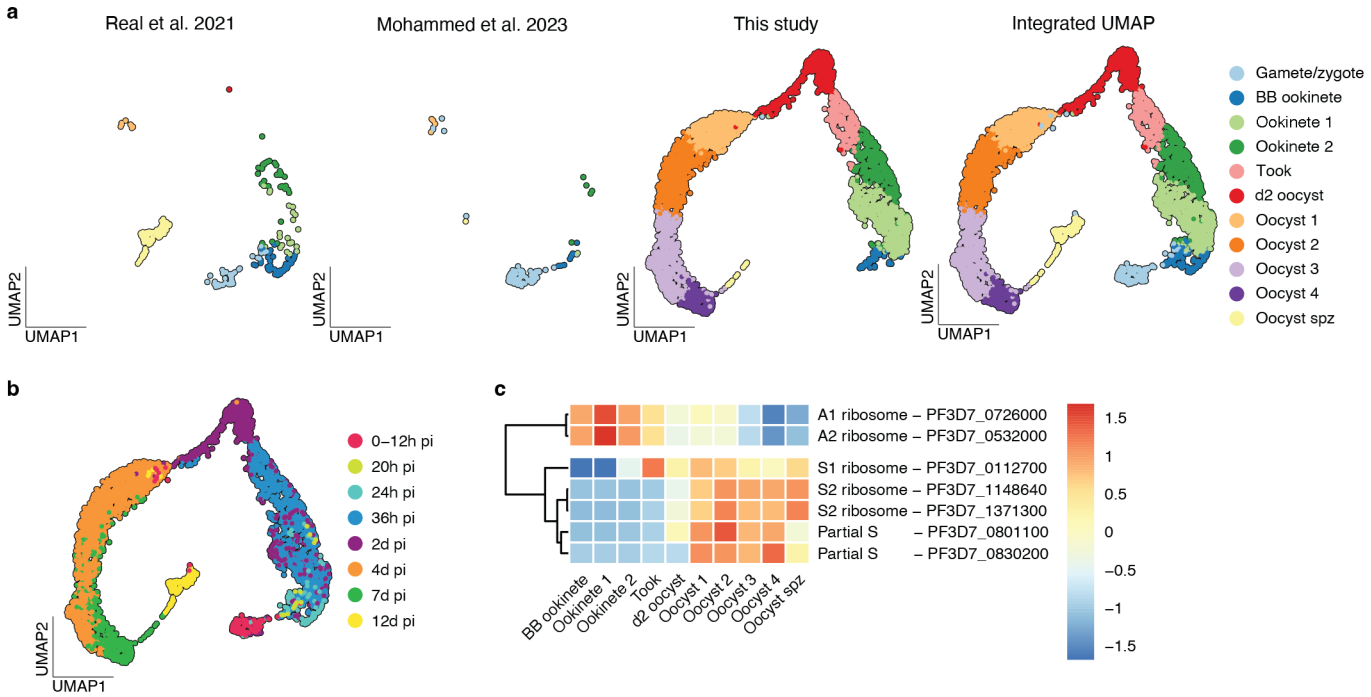

Supplementary Figure 3 | Integrated *P. falciparum* UMAPs across data origin and time
a-b, UMAP plots representing the integrated data of *P. falciparum* (**a**) split by their study of origin and (**b**) colored by timepoints of single cell collection. **c,** Heatmap showing the Z scores of expression patterns of ribosomal RNA (rRNA). Each row represents a cumulative expression of 18S (when present), 5.8S and 28S for each rRNA type (A1, A2, S1, S2). The gene ID given is of the corresponding 28S.

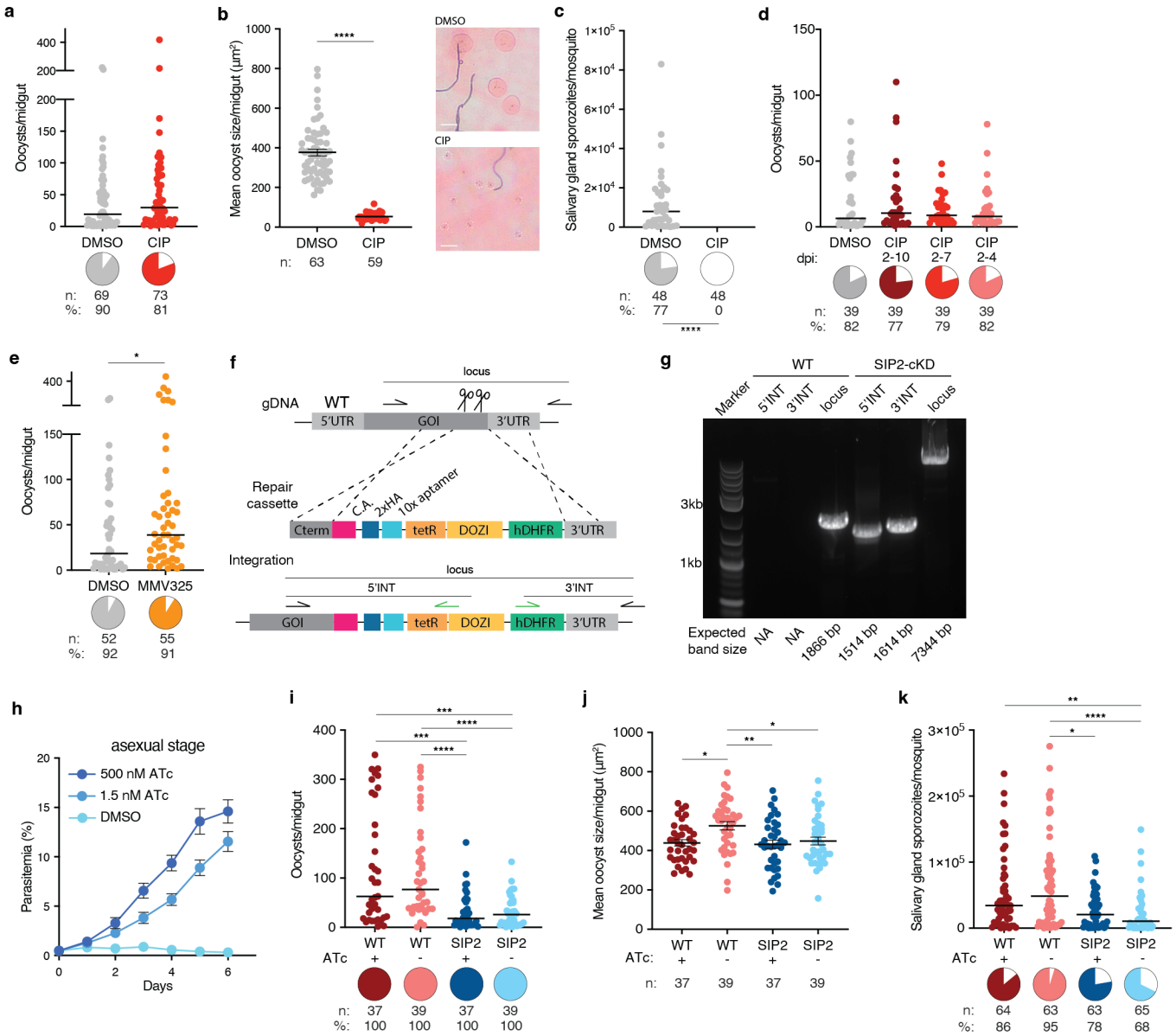

Supplementary Figure 4 | Functional validation of candidate genes in oocyst growth and sporozoite infection
a-c, CIP delivery via sugar solution 2-10d pi (**a**) had no effect on oocyst prevalence (pie charts, Fisher's exact test, two-tailed) or intensity (Mann-Whitney test, two-tailed) at 7d pi, but (**b**) significantly reduced oocyst size (unpaired t-test, two-tailed; top image is representative of control oocysts, bottom image representative of CIP oocysts. Scale bar: 20 µm) and (**c**) produced no sporozoites in salivary glands at 14d pi (Fisher's exact test, two-tailed). **d,** CIP exposure for 3 different treatment durations had no effect on oocyst prevalence (pie charts, chi-squared, two-tailed) or intensity (Kruskal-Wallis test, Dunn's correction). **e,** MMV325 delivery via sugar solution from 2-10d pi had no effect on oocyst prevalence at 7d pi (pie charts, pairwise two-sided chi-squared test), though it slightly increased oocyst intensity (Mann-Whitney test, two-tailed). **f,** Scheme (not to scale) of the *Pf*SIP2 conditional knockdown (cKD) construct. Positions of primer pairs for integration validation are indicated. **g,** PCR amplifications of the 5' and 3' integrated regions (5'INT and 3'INT) and locus in WT NF54 and *Pf*SIP2-cKD parasites, demonstrating the absence of WT parasites in the cKD line. **h,** *Pf*SIP2 knockdown by ATc withdrawal in the asexual blood stage led to parasite death (two-way ANOVA, Dunn's correction). **i-k,** PfSIP2 knockdown by ATc withdrawal had no effect on (**i**) oocyst prevalence (pairwise two-sided chi-squared test), intensity (Kruskal-Wallis test, Dunn's correction), and (**j**) size (one-way ANOVA, Dunn's correction) at 7d pi, and had no effect on (**k**) prevalence and intensity of salivary gland sporozoites at 14d pi (Kruskal-Wallis test, Dunn's correction and pairwise two-sided chi-squared test). Data are represented as mean ± SEM in panels **b, h,** and **j**, and as median in panels **a, c, d, e, i,** and **k**. *n* indicates the number of mosquitoes. *p < 0.05, **p < 0.01, ***p < 0.001, ****p < 0.001.

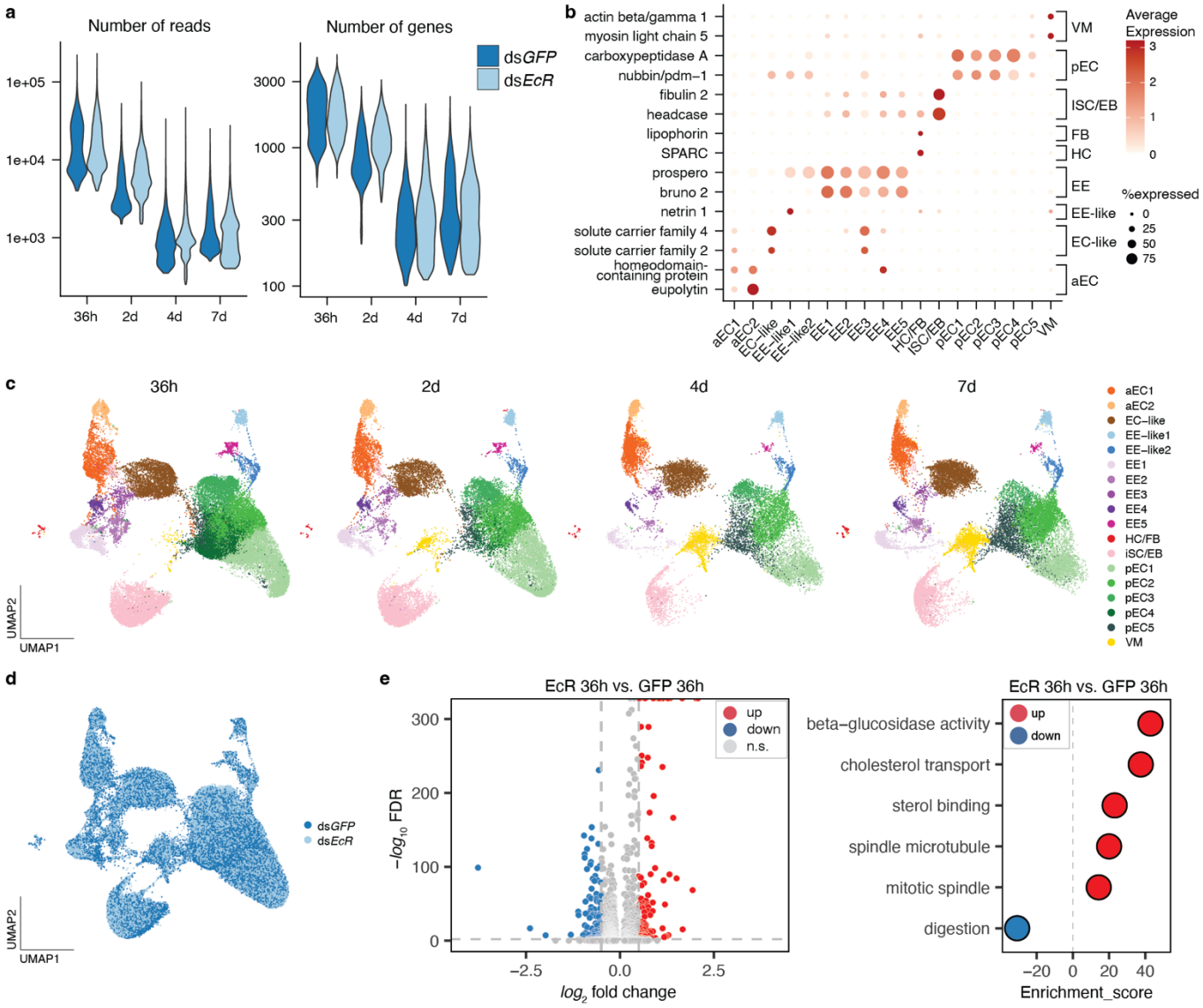

Supplementary Figure 5 | Quality control and clustering of the *An. gambiae* scRNA-seq data
a, Violin plots displaying key metrics for the mosquito scRNA-seq datasets (total numbers of reads, left, and genes, right) after QC. **b**, Dot plot displays cell type-specific markers, showing their average expression (color) and the proportion of parasites expressing each marker (size). Cell types shown are anterior enterocytes (aEC), enteroendocrines (EE), hemocytes (HC), fat body (FB), intestinal stem cells/enteroblasts, (ISC/EB), posterior enterocytes (pEC) and visceral muscles (VM). **c**, UMAPs of *An. gambiae* cells split by timepoints, showing the dynamic changes of the midgut cell population shortly after blood digestion (36h and 2d pi) and when subsequently maintained on sugar-only diet (4d and 7d pi). **d**, UMAP of the *An. gambiae* single cell transciptomes shows good overlap between the two treatments (ds*EcR* or ds*GFP*). **e**, Differential gene expression comparison between ds*EcR* and ds*GFP* mosquitoes at 36h pi, after binning by cell cluster (left) and the corresponding enriched GO terms for regulated genes (right).

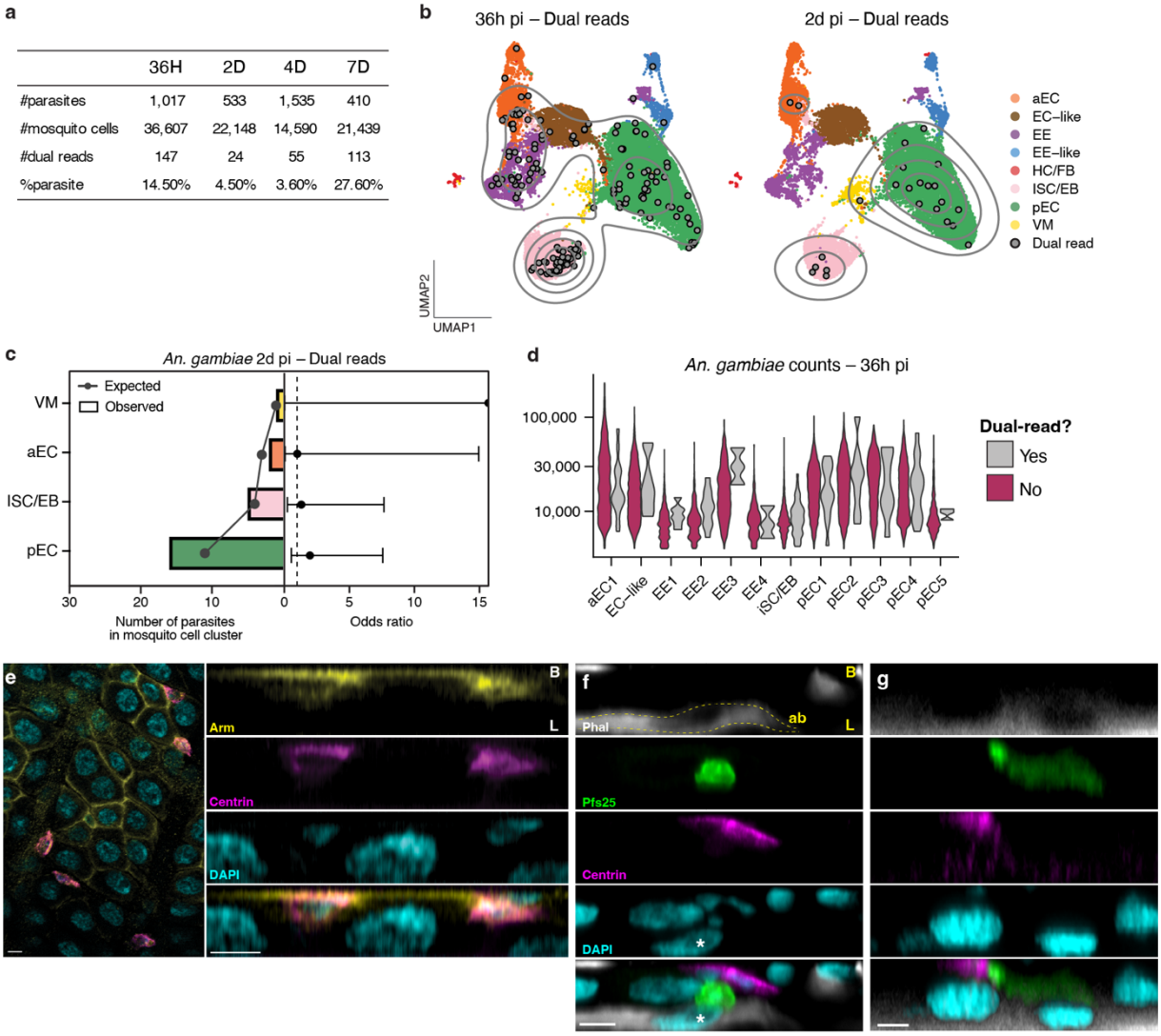

Supplementary Figure 6 | Dual-read parasites at 36h pi show an association with intestinal progenitor cells
a, Table summarizing the number of parasites, mosquito cells, and dual read parasites, as well as the percentage of dual-read parasites and cells collected at each timepoint. **b,** *An. gambiae* UMAPs at 36h and 2d pi colored by cell type and overlaid with dual-read cells (gray circles) and contour lines (light gray lines) displaying the density of dual-read cells. **c,** Statistical analysis of the distribution of dual-read parasites in mosquito cell types at 2d pi, showing the observed vs. expected numbers if the distribution were random (left x-axis) and resulting odds ratio (right x-axis) (Fisher exact test, two-tailed). **d,** Violin plot showing similar amount of reads in mosquito cells regardless of whether they are dual-read cells. **e,** Maximum intensity projection from confocal imaging (9.66 µm Z-stack) showing that centrin (magenta) antibody stains mosquito midgut progenitor cells located on the basal side of the midgut (B, top) and co-localizes with the well-characterized ISC marker, armadillo (Arm, yellow). **f-g,** Confocal imaging of parasites traversing the mosquito midgut epithelium at 36h pi. (**f**) Parasites (Pfs25, green) were found to point towards a progenitor cell (centrin, magenta) directly above an extruding cell (asterisk, nucleus of the extruded cell) found between the two actin brushes (ab, yellow dashed line) delimiting each epithelium (see also supplementary video 1). (**g**) Other ookinete left a Pfs25 trail into a large cell reminiscent of an enterocyte. Phalloidin (phal, gray) was used to define the basal side (B, top) and the luminal brush border (L, bottom), and nuclei were stained with DAPI (cyan). Scale bar: 5 µm.

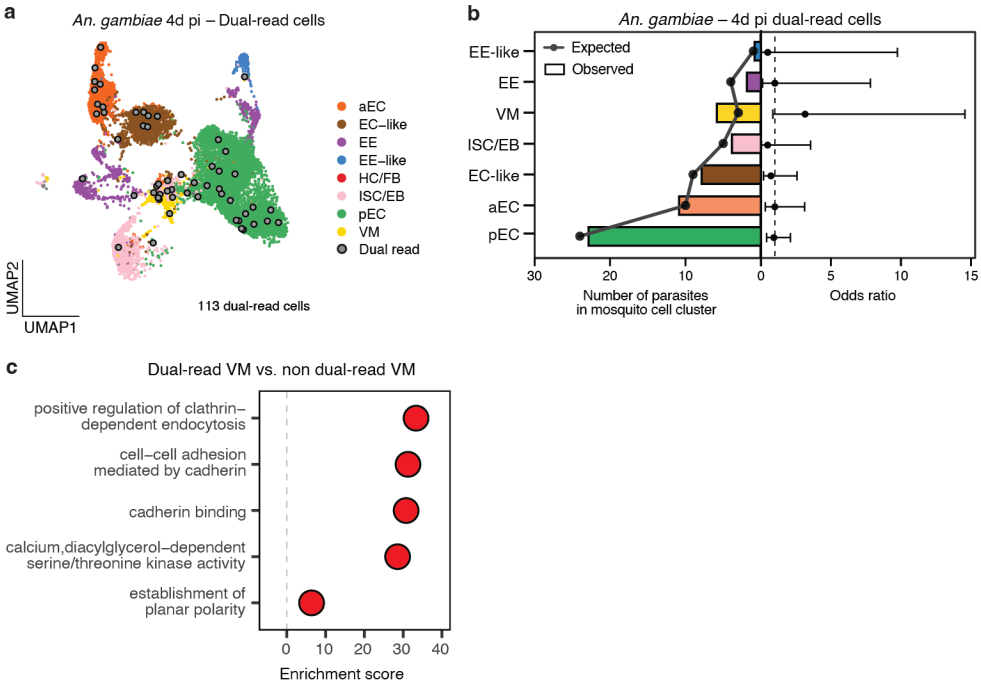

Supplementary Figure 7 | Unlike at 7d pi, dual-read parasites at 4d pi are not associated with mosquito cells
a, *An. gambiae* UMAPs at 4d pi colored by cell types and overlaid with dual-read cells (gray circles). **b,** Statistical analyses of the distribution of dual-read parasites in mosquito cell types at 4d pi showing the observed vs. expected numbers if the distribution were random (left x-axis) and resulting odds ratio (right x-axis) (Fisher exact test, two tailed). **c**, Functional enrichment analysis (Fisher's one-tailed test) of the genes upregulated in VM cells associated with a parasite at 7d pi compared to non-dual-read cells. *Drosophila melanogaster* orthologs were used for the analysis as most of the upregulated *An. gambiae* genes were not functionally annotated.